Cosmological Aspects of

Gamma Ray Bursts

by

Razieh Behkam

A Thesis Presented in Partial Fulfillment
of the Requirements for the Degree
Doctor of Philosophy

Approved November 2010 by the
Graduate Supervisory Committee:

Rogier Windhorst, Chair
James Rhoads
Bing Zhang
Cecilia Lunardini
Lawrence Krauss

ARIZONA STATE UNIVERSITY

December 2010

ABSTRACT

Gamma-ray burst observations provide a great opportunity for cosmography in high redshift. Some tight correlations between different physical properties of GRBs are discovered and used for cosmography. However, data selection, assumptions, systematic uncertainty and some other issues affect most of them. Most importantly, until the physical origin of a relation is understood, one should be cautious to employ the relation to utilize Gamma ray bursts for cosmography.

In the first part of this dissertation, I use Liang-Zhang correlation to constrain Λ Cold Dark Matter standard cosmology and a particular class of brane cosmology (brane-induced gravity model). With the most probable model being $\Omega_m = 0.23$ and $\Omega_\Lambda = 0.77$ for flat ΛCDM cosmology and $\Omega_m = 0.18$ and $\Omega_{r_c} = 0.17$ for flat brane-induced gravity cosmology, my result for the energy components of these two models is comparable with the result from SNIa observation. With average uncertainty of distance modulus being 0.2771, the two discussed cosmologies are indistinguishable using my current sample of GRB with redshift ranging between 0.1685 and 3.2. I argue that by expanding my sample and adding more low and high redshift GRBs and also with improvement in using GRB for cosmography, we might be able to distinguish between different cosmological models and tighten the most probable model.

Looking into correlation and evolution of GRB prompt emission and afterglow has many advantages. It helps to open windows to comprehend the physics of GRBs and examine different GRB models. It is also possible to use GRB

correlation as an accurate redshift estimator and more importantly to constrain the cosmological parameters. XRT flares of GRB afterglow are thought to be the result of central engine activity. Studying this component leads us to understand GRB flare and central engine nature. In the next part of this dissertation, I study the correlation and evolution of different prompt emission and afterglow GRB properties and some GRB flare-based quantities. Considering instrument bias and selection effect, I conclude some well-correlated correlations and establish some property evolution. The correlation between average luminosity and isotropic γ-ray energy, energy of plateau and isotropic γ-ray energy and luminosity at break time and break time and evolution of plateau energy are well established. It is also realized that the apparent evolution of isotropic γ-ray energy and average luminosity is due to the instrumental flux threshold. With expanding the sample of GRB and accommodating more GRBs with XRT flares to my sample, I can reevaluate my result more firmly and confirm or rule out some hard to assert results due to limited number of data.

In search for physically motivated GRB relation, analyzing the thermal component of GRB prompt emission, I derive two well-correlated relations. They are between calculated and estimated flux of the GRB thermal component for the co-moving bolometric and co-moving detector band-pass range of spectrum. In this study, three samples of Swift, pre-Swift and combined samples are used. The quality of this correlation is comparable with the Ghirlanda relation in terms of Spearman rank correlation parameters (correlation coefficient and correlation

significance) and reduced $\chi^2$of best fit. These results for the Swift GRB sample for co-moving bolometric range of spectrum are 0.81, 4.07×10^{-7} and 0.66 respectively. The derived correlations also imply a $E_{\gamma,iso} - E_{peak}^4$ relation that provides physical insight to $E_\gamma - E_{peak}$ Ghirlanda correlation. Three scaling coefficients are employed to study these correlations. Monte Carlo statistics indicates that the existing correlations are independent of these constants. For Swift and combined sample 73% - 84.8% successes are recorded. Therefore, it is expected by determining these constants, the tightness of these correlations will further improve.

DEDICATION

This dissertation is dedicated to my parents, Maryam and Seyed Asadollah Behkam, for their continuous unconditional love, support and encouragement and for instilling the importance of hard work and higher education.

ACKNOWLEDGMENTS

First and foremost, I am thankful to God for the power to think and all other blessings in my life. I am grateful to my parents, Maryam and Seyed Asadollah Behkam, for supporting me along the way. I owe my deepest gratitude to them for providing me opportunity to pursue my dreams and bearing our parting. This would not have been possible without the loving support of my dear husband, Seyed Esmael Delpassand. I am beholden to him to support me through this journey. I offer my heartfelt gratitude to him and our daughter, Raya Delpassand, for their understanding and patience. I thank my sister, Bahareh Behkam, and my brother, Reza Behkam, for their support and encouragement.

I thank my advisor, Prof. Rogier Windhorst, for trusting me and providing me opportunity to work on a subject that I enjoy the most. Prof. James Rhoads truly served as a secondary advisor. He taught me about the field of GRB, as I was new to the field and guided me along the way with his valuable insight and experience. I am grateful to him. I thank Prof. Bing Zhang for giving me a chance to work with him and his research group and learning technical details of how to study Gamma ray bursts.

I thank my whole committee for doing their part to make this process worthwhile. They are Prof. R. Windhorst, Prof. J. Rhoads, Prof. B. Zhang, Prof. C. Lunardini and Prof. L. Krauss. I also thank Dr. R. Jansen for contributing his time to be present for my oral comprehensive exam and my defense.

I thank my fellow graduate students particularly Kazuyuki Tamura, Russell Ryan and Robert Morgan from Arizona State University and Binbin Zhang from the University of Nevada at Las Vegas for being supportive throughout the way. I also benefited from knowledge and experience of Dr. Enwei Liang in the Gamma ray burst field. I also appreciate Robert Morgan for his time and his comments regarding the manuscript of my dissertation.

Finally, I thank Arizona State University and the Department of Physics for hosting me throughout this process.

TABLE OF CONTENTS

Page

LIST OF TABLES

Table Page

LIST OF FIGURES

Figure Page

Chapter 1

A REVIEW ON GAMMA RAY BURST

Gamma ray bursts first were discovered in the late 1960s. GRBs are electromagnetic signals that have most of their output in gamma-ray band at sub Mev energies. They have a short duration of only tens of seconds. CGRO, Swift and Fermi are three missions that provide us great information about these phenomena. Table 1.1 shows the telescopes on board of these satellites with their energy ranges.

Table 1.1. GRB missions

Mission	Telescope	Energy range
CGRO (1991-2000)	BATSE	20kev-1000kev
	OSSE	50kev-10Mev
	COMPTEL	1Mev-10Mev
	EGRET	20Mev-30Gev
Swift (2004-present)	BAT	15kev-150kev
	XRT	0.2kev-10kev
	UVOT	170nm-600nm
Fermi (2008-present)	LAT	20Mev-300Gev
	GBM	8kev-30Mev

Swift and Fermi are two ongoing missions at present. Swift is named after a bird, which chases after insects. Swift is like a quick, small satellite that points here and

there to chase after GRBs. Swift instruments pick up x-ray and optical emission. On the other hand, Fermi (formerly GLAST) looks over the whole sky all the time and is designed to pick up at the upper end of the Swift range and beyond.

In this chapter, a background on GRB phenomena is reviewed. First, different GRB components are introduced and their temporal and spectral properties are discussed. Then, I briefly look at physics of GRBs. Next, two early indications for cosmological origin of GRBs are discussed. In chapter 2, I use Liang-Zhang relation to constrain ΛCDM standard cosmology and brane-induced gravity cosmology model. In this chapter, I briefly review a background on these two cosmological models and discuss the formalism and result of the method to constrain the energy components of these models using GRB observation. In chapter 3, I analyze Swift XRT data and examine different GRB properties. Then, GRB property correlations and their evolution are studied. In the last chapter, it is shown how I employ the properties of thermal component of GRB prompt emission to deduce well-correlated relations. I also argue how these relations give physical insight to the Ghirlanda relation. At present, this relation is widely used for cosmography. In the last section of each chapter, a prospect for future of the work is provided.

1.1 Gamma Ray Bust components

Gamma ray burst consists of two components: prompt emission and afterglow. In this section, first a review of different temporal and spectral properties of these two components is given.

Prompt emission light curve happens in gamma-ray band. It is very irregular and erratic with spiky components. A typical light curve of a BATSE GRB is shown in Figure 1.1 (Fishman et al. 1995).

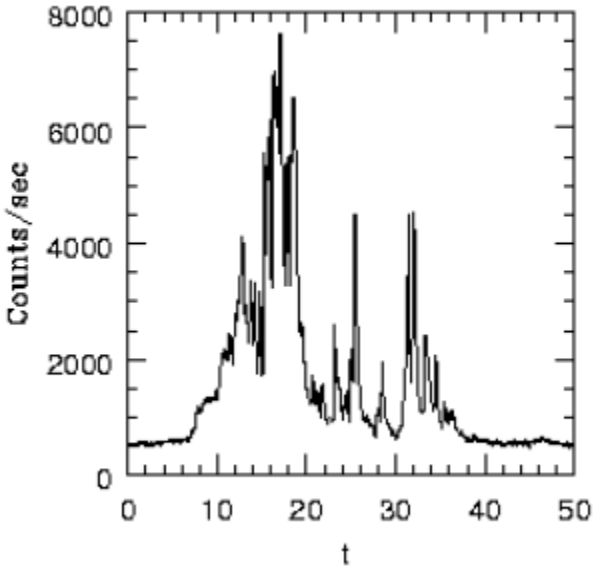

Figure 1.1. A typical light curve of a BATSE GRB (Fishman et al. 1995).

On the other hand, afterglows are broadband, detected in the x-ray, the optical/infrared and the radio band. X-ray afterglow is the most commonly detected. X-ray light curve consists of four power law segments: steep decay, shallow decay, normal decay, a fourth segment and a flaring component (Figure 1. 2).

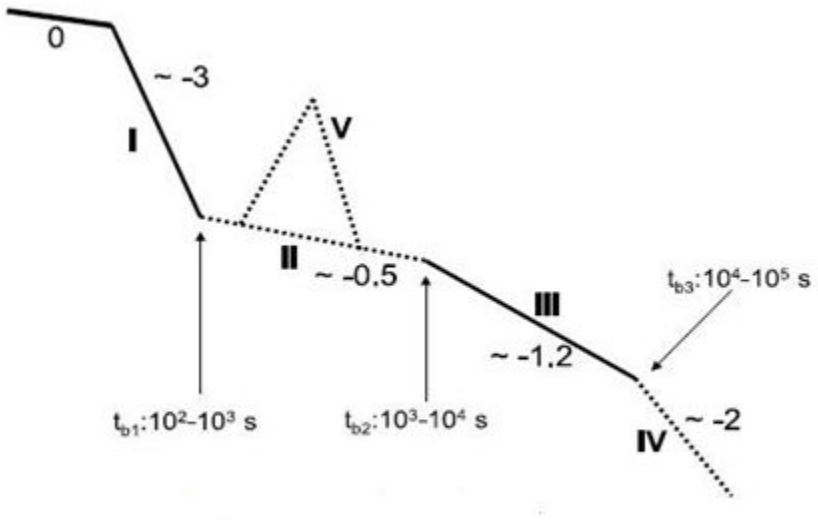

Figure 1.2. A synthetic x-ray light curve based on the observational data from the Swift XRT. (Zhang et al. 2006)

Prompt emission lasts tens of seconds. GRB duration usually is defined as the time interval within which 90% of the burst fluence is detected (T_{90}). T_{90} span 5 orders of magnitude, from 10^{-2} to 10^3 s. The distribution of duration of GRBs is bimodal. The bimodal distribution of duration of the BATSE GRBs is shown in figure 1. 3. Based on this distribution, GRBs are categorized by their duration. GRBs with duration less than 2s are considered short and GRBs with duration greater than 2s are considered long. The typical duration of short GRBs is 0.2s. They consist of about 25% of GRB population and most of their output is in the soft range of gamma-ray band. The typical duration of long GRBs is 20 s. They

consist of about 75% of GRB population and most of their output is in hard range of gamma-ray band. Short GRB are thought to be originated from the merger of binary neutron stars while long GRBs are associated with the death and collapse of massive stars. The typical value for GRB afterglow is 10^5 s.

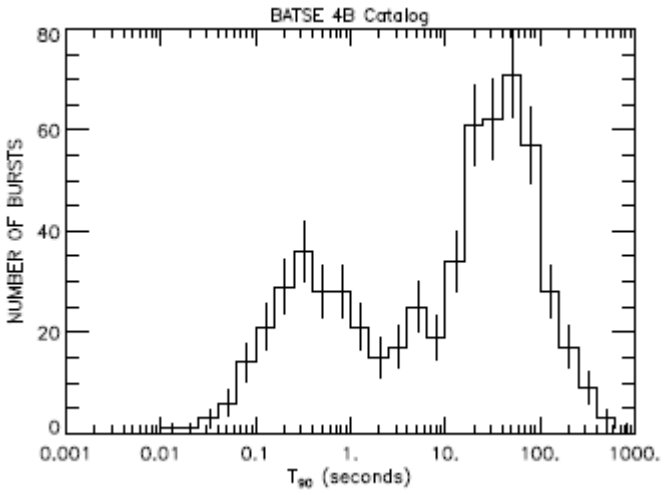

Figure 1.3. The bimodal distribution of duration of the BATSE GRBs. (Paciesas et al. 1999)

Initially, prompt emission spectrum was considered non-thermal. Example of prompt emission spectrum is shown in figure 1. 4. The prompt emission spectrum is commonly fitted with a smooth broken power law, known as the Band function.

$$\varphi(E) = \begin{cases} \left(\frac{E}{100kev}\right)^{\alpha} exp\left(-\frac{E}{E_0}\right) & (\alpha-\beta)E_0 \geq E \\ \left[\frac{(\alpha-\beta)E_0}{100kev}\right]^{(\alpha-\beta)} exp(\beta-\alpha)\left(\frac{E}{100kev}\right)^{\beta} & (\alpha-\beta)E_0 \leq E \end{cases}$$

α is low energy photon spectral index, β is high energy photon spectral index and E_0 is the transition energy. Transition energy, E_0, is related to Peak energy of the spectrum, E_p, by

$$E_0 = \frac{E_p}{2+\alpha}$$

Typical values of α and β are -1±1, -2^{+1}_{-2} respectively and E_p typically ranges between 50 and 250kev.

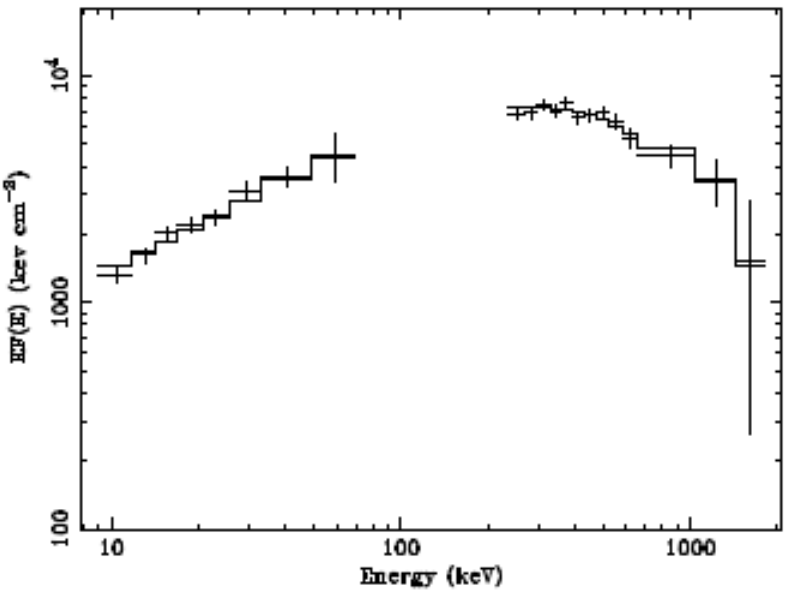

Figure 1.4. Example of prompt emission spectrum. (Amati et al. 2002)

Ryde et al. (2002) interprets the prompt emission spectrum as composite of a thermal and a non-thermal component (figure 1.5). We discuss this discovery and study the thermal component of prompt emission spectrum with more details in chapter 4.

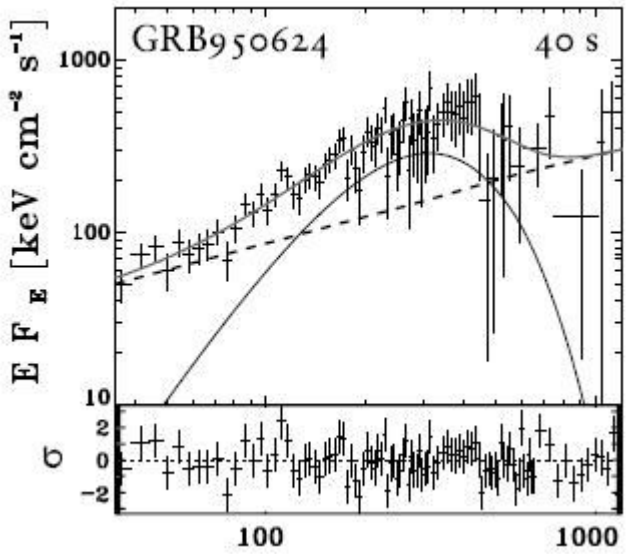

Figure 1.5. An example of time resolved spectrum, observed by BATSE, fitted with the two-component model: composite of a thermal and non-thermal component. (Ryde 2005)

Afterglow continuum spectrum follows a power law.

$$F_\upsilon \propto \upsilon^{-\beta}$$

where β is a constant and ν is frequency. The optical afterglow of spectrum of GRB030329 is shown in figure 1. 6. In chapter 4, we introduce more properties of GRBs and study their correlation and evolution.

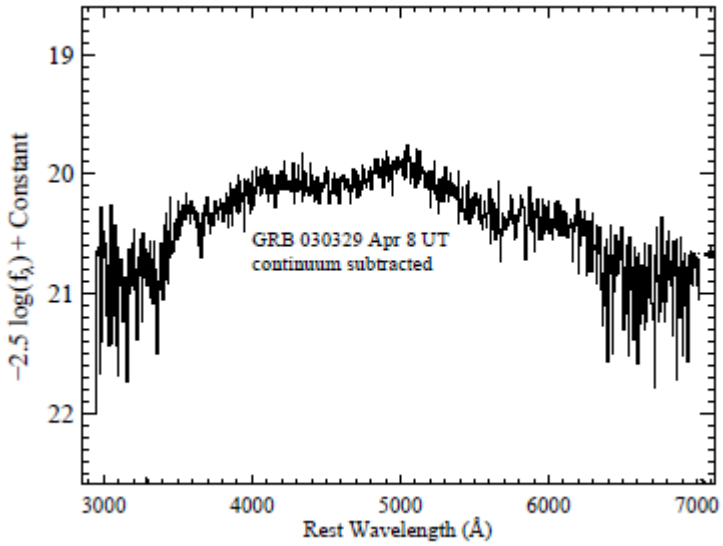

Figure 1.6. The optical afterglow spectrum of GRB 030329. (Stanek et al. 2003)

1.2 GRB relativistic expansion

GRBs emit photons with very high energies. If the expansion is non-relativistic, the optical depth, τ, of photons would be too large and photons could not be observed. This is called the compactness problem (Piran et al. 1999). The solution is that the GRB explosion expansion is relativistic with a lower limit on the Lorenz factor, γ. Three processes contribute to the optical depth of high energy photons. They are annihilation of photon pairs, scattering of photon by e^+ or e^- of another annihilation and scattering of photon by baryon election. In all these three processes, for GRBs to be optically thin and decrease optical depth, a lower limit

on Lorentz factor is required (Blandford et al. 1996; Lithwick et al. 2001). This lower limit shows that the expansion should be relativistic.

1.3 GRB Standard fireball shock model

As it is discussed in the last section, GRB material must move relativistically. This is the first element of any GRB model. The dynamics of gamma ray burst can be understood independently from any uncertainty about their progenitors. GRBs are thought to be the result of a cataclysmic event leading to a relativistically expanding fireball. (Cavallo et al.; Meszaros et al. 1999)

1.4 GRBs have cosmological origin

BATSE observation in 1991 indicated that GRBs have isotropic and homogenous distribution and GRB redshift measurement in 1997 showed that they are at cosmological distance. These two evidences confirmed that GRBs have cosmological origin.

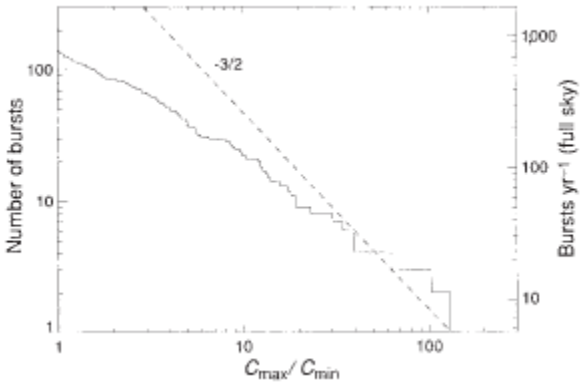

Figure 1.7. The number of bursts vs. intensity distribution. (Meegan et al. 1992)

Meegan et al. (1992) shows that the number of bursts versus intensity distribution does not quit follow -3/2 power law expected for a spatially extended homogenous distribution (Figure 1.7).

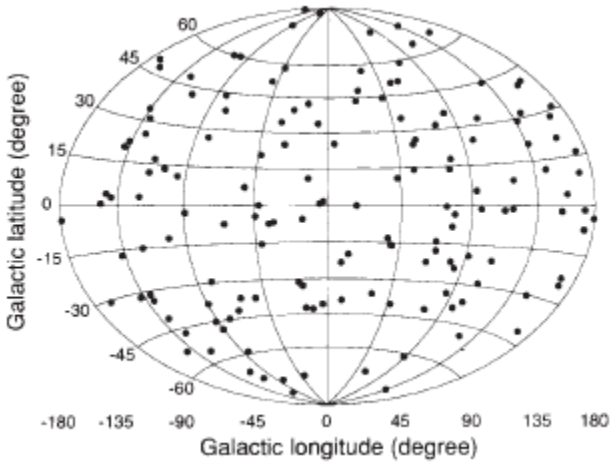

Figure 1.8. The angular distribution of 153 bursts in galactic coordinates. (Meegan et al. 1992)

However, the angular distribution of 153 BATSE bursts in galactic coordinates shows no significant deviation from isotropy (Figure 1.8). Considering these two evidences, Meegan et al. (1992) argues that these result are inconsistent with the spatial distribution of any known population of galactic object, but may be consistent with the bursts being at cosmological distances. Metzger et al. (1997)

discovered that OTJ065340+79163 is considered the optical counterpart to GRB970508. The spectrum of OTJ065349 is shown in Figure 1.9.

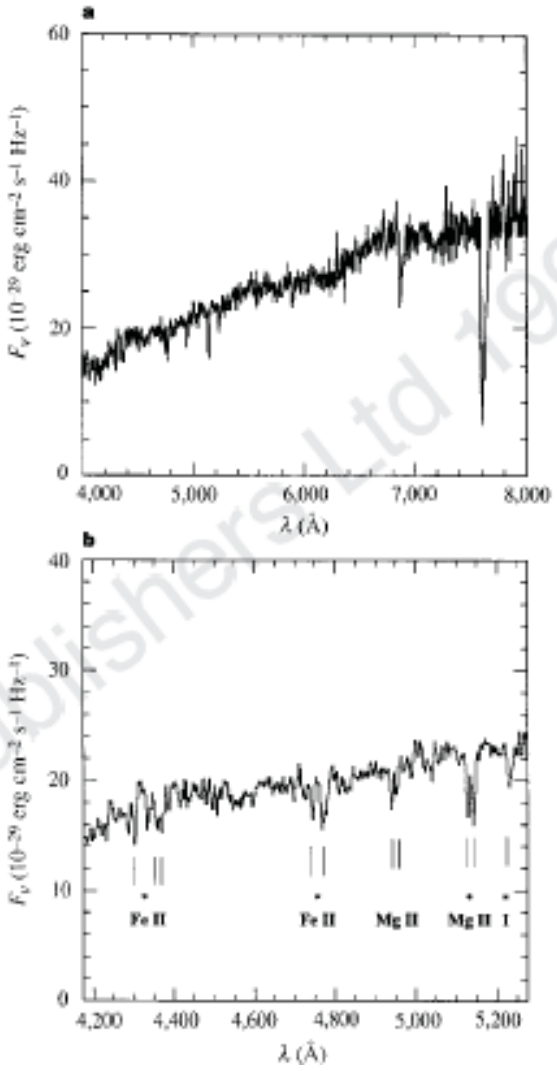

Figure 1.9. The spectrum of OTJ065349+79163. (Metzger et al. 1997)

The lines with asterisk were identified with absorption line of some redshift known systems. Table 1.2 shows OTJ065349+79163 absorption lines. The presence of absorbing system along the line of sight at z=0.835 indicates that its gamma ray burst counterpart GRB70508 is at cosmological distance.

Table 1.2. OTJ065349+79163 absorption lines. (Metzger et al. 1997)

λ_{obs} (Å)	Unc.	W_λ (Å)	Unc.	λ_{rest} Å	z	Assignment
4,302.5	1.8	1.3	0.3	2,344.2	0.8354(8)	Fe II
4,359.7	1.4	1.3	0.3	2,374.5	0.8360(6)	Fe II
4,372.2	1.5	1.4	0.3	2,382.8	0.8349(6)	Fe II
4,746.7	1.7	1.0	0.4	2,586.7	0.8350(7)	Fe II
4,769.7	1.3	2.3	0.2	2,600.2	0.8344(5)	Fe II
4,941.1	1.5	1.3	0.3	2,796.4	0.7670(5)	Mg II
4,953.9	1.5	1.0	0.4	2,803.5	0.7670(5)	Mg II
5,130.4	1.1	2.7	0.2	2,796.4	0.8346(4)	Mg II
5,144.0	1.1	3.0	0.2	2,803.5	0.8348(4)	Mg II
5,232.6	1.3	1.8	0.2	2,853.0	0.8341(5)	Mg I

In chapter 2, it is presented how GRBs may be used for cosmography.

Chapter 2

CONSTRAIN FROM GRB OBSERVATION FOR COSMOLOGICAL MODELS

Early attempts to constrain cosmological models using GRB energies were unsuccessful (Dermer et al. 1992; Rutledge et al. 1995; Cohen et al. 1997). That is due to the wide distribution, more than three order of magnitude, for isotropic gamma energy and luminosity (Bloom et al. 2001).

The realization that GRB is a jetted phenomenon led to the discovery that the collimation-corrected gamma ray prompt emission is nearly constant and can be used for cosmography.

Bloom et al. (2003) with their sample of 29 redshift-known GRBs shows that the apparent constancy of the geometry-corrected gamma-ray prompt emission energy is due to the lack of homogeneity in the current 17 GRB sample of Frail et al. (2001). They showed that this constancy is the result of compromising 20% of their GRB sample with energies spanning three orders of magnitude.

The correlation between collimation-corrected gamma-ray prompt emission energy, E_γ, and the peak energy in the rest frame prompt emission spectrum, E_p, known as the Ghilanda relation is one of the less widely scattered GRB correlations which is widely accepted and used as standard candle (Ghirlanda et al. 2004; Friedman et al 2005; Ghirlanda 2009).

Although this correlation is a well-correlated relation, it strongly depends on some assumptions. The most important assumptions are the unknown density of

the circumburst medium, the efficiency of converting explosion energy to γ-ray, data selection choices for individual bursts and assumptions in error analysis (Friedman 2005).

The Liang-Zhang relation (Liang et al. 2005) is a relation between isotropic γ-ray prompt emission energy and rest frame peak energy of prompt emission spectrum and rest frame break time of afterglow light curve.

In Liang-Zhang relation isotropic gamma-ray prompt emission energy is involved rather than geometry-corrected gamma-ray involved in the Ghirlanda relation. Therefore, the two assumptions related to the geometry-corrected γ-ray energy calculation are eliminated. These two assumptions consist of the unknown density of the circumburst medium and the efficiency of converting explosion energy to γ-rays.

Therefore, here I use the Liang-Zhang relation to constrain two cosmological models the ΛCDM standard model and the Brane-induced gravity model. In section 2.2, I review a brief definition of these two models and their cosmological dynamics. In section 2.3, the formalism that is used to utilize the Liang-Zhang relation for cosmography is discussed. In section 2.4, I discuss the results and conclude in section 2.5. The prospect for this work is also addressed in this section.

2.1 Lambda Cold Dark Matter versus Brane Induced Gravity Model

Here a brief definition of these two models and their cosmological dynamics is

reviewed.

The **Λ**CDM model is frequently referred to as the concordance model of big bang cosmology. Lambda stands for the cosmological constant that is an energy component with negative pressure and allows the late time accelerated expansion of the universe. CDM stands for Cold Dark Matter where the dark matter is explained as being cold. In this model, our universe is four dimensional.

The Brane-induced gravity model is a particular class of brane world models. In this model our four dimensional universe is a membrane (called brane) embedded into a higher (five) dimensional bulk space-time (Dvali 2000). This model explains the late time acceleration of the universe through a large scale modification of gravity known as leakage of gravity into extra dimension that causes weaker gravity at cosmological distance (Deffayet 2001).

In **Λ**CDM standard cosmology model, for a given content of the universe with total energy density ρ (and pressure p), the first Friedman's equation is

$$H^2 + \frac{k}{a^2} = \frac{\rho}{3M_{pl}^2} \tag{2.1}$$

where $k = -1,0,1$ is curvature and a is scaling factor and M_{pl} is plank mass. The energy-momentum conservation equation for this model is

$$\dot{\rho} + 3H(p + \rho) = 0 \tag{2.2}$$

where

$$H \equiv \frac{1}{a}\frac{da}{dt} \tag{2.3}$$

is the Hubble constant of the universe.

In the brane-induced gravity model, the first Friedman's equation is replaced by

$$H^2 + \frac{k}{a^2} = \left(\sqrt{\frac{\rho}{3M_{pl}^2} + \frac{1}{4r_c^2}} + \frac{1}{2r_c} \right)^2 \tag{2.4}$$

where r_c is crossover scale and defined by

$$r_c = \frac{M_{Pl}^2}{2M_{(5)}^3} \tag{2.5}$$

and $M_{(5)}$ is the 5D reduced plank mass. In the limit where $\rho/M_{pl}^2 \gg 1/r^2$, (2.4) results in the first Friedman's equation for **Λ**CDM standard cosmology model and when $\rho/M_{pl}^2 \ll 1/r^2$the result is the de Sitter solution. The energy-momentum conservation equation is the same as the one for the ΛCDM model.

In **Λ**CDM model the Hubble parameter is

$$H^2(z) = H_0^2 \{ \Omega_k (1+z)^2 + \Omega_M (1+z)^3 + \Omega_\alpha (1+z)^{3(1+\omega_\alpha)} \} \tag{2.6}$$

where z is the redshift and the normalization factor is

$$\Omega_k + \Omega_M + \Omega_\alpha = 1 \tag{2.7}$$

While in the brane-induced gravity model, the Hubble parameter is

$$H^2(z) = H_0^2 \left\{ \Omega_k (1+z)^2 + \left(\sqrt{\Omega_{r_c}} + \sqrt{\Omega_{r_c} + \sum_\alpha \Omega_\alpha (1+z)^{3(1+\omega_\alpha)}} \right)^2 \right\} \tag{2.8}$$

and the normalization factor is

$$\Omega_k + \left(\sqrt{\Omega_{r_c}} + \sqrt{\Omega_{r_c} + \sum_\alpha \Omega_\alpha} \right)^2 = 1 \tag{2.9}$$

Ω's of matter and curvature are defined in the usual way by

$$\Omega_\alpha \equiv \frac{\rho_\alpha^0}{3M_{Pl}^2 H_0^2 a_0^{3(1+\omega_\alpha)}} \tag{2.10}$$

$$\Omega_k \equiv \frac{-k}{H_0^2 a_0^2} \tag{2.11}$$

ρ_α^0 is the energy density of different components labeled by α with constant equation of state parameters ofω_α. The index, 0 , shows the current value of the quantity.

2.2. Formalism

Here, I use Liang-Zhang relationship (Liang et al. 2005) and perform regression analysis for a their sample of 15 gamma ray bursts (table 2.1) to search a possible empirical relation among three observables: $E_{\gamma,iso}$, $E_p'$and t_b' . $E_{\gamma,iso}$, $E_p'$and t_b' are isotropic γ-ray energy, restframe peak energy and rest frame break time respectively. Where

$$E_p' = E_p(1+z) \tag{2.12}$$

$$t_b' = \frac{t_b}{(1+z)} \tag{2.13}$$

The data is shown in table 2.1 with the following heading: (1) GRB name; (2) redshift; (3) redshift error; (4) spectral peak energy; (5) spectral peak energy error (6) low-energy spectral index; (7) low-energy spectral index error; (8) high-energy spectral index; (9) high-energy spectral index error; (10) γ-ray fluence; (11) γ-ray fluence error; (12) lower limit of BAT detector band-pass; (13) higher limit of BAT detector band-pass; (14) afterglow break time between shallow and normal segment; (15) break time error.

Table2.1. GRB data table .

name	z	σ_z	E_p kev	σ_{E_p} kev	α	σ_α	β	σ_β	S_γ $ergscm^{-2}$	σ_{S_γ} $ergscm^{-2}$	e_1 kev	e_2 kev	t_b days	σ_{t_b} days
(1)	(2)	(3)	(4)	(5)	(6)	(7)	(8)	(9)	(10)	(11)	(12)	(13)	(14)	(15)
980703	0.966	0.0009	254	50.8	-1.31	0.26	-2.396	0.265	22.6	2.3	20	2000	3.4	0.5
990123	1.6	0.0008	780.8	61.9	-0.89	0.08	-2.45	0.97	300	40	40	700	2.04	0.46
990510	1.62	0.0015	161.5	16.1	-1.23	0.05	-2.70	0.4	19	2	40	700	1.6	0.2
990712	0.43	0.0004	65	11	-1.88	0.07	-2.48	0.56	6.5	0.3	40	700	1.6	0.2
991216	1.02	0.0009	317.3	63.4	-1.234	0.095	-2.184	0.265	194	19	20	2000	1.2	0.4
011211	2.14	0.001	59.2	7.6	-0.84	0.09	-2.30	0.265	5.0	0.5	40	700	1.56	0.02
020124	3.2	0.004	86.9	15.0	-0.79	0.15	-2.30	0.265	8.1	0.8	2	400	3	0.4
020405	0.69	0.0009	192.5	53.8	0.00	0.25	-1.87	0.23	74.0	0.7	15	2000	1.67	0.52
020813	1.25	0.0009	142	13	-0.94	0.03	-1.57	0.035	97.9	10	2	400	0.43	0.06
021211	1.006	0.0009	46.8	5.5	-0.86	0.1	-2.18	0.2	3.5	0.1	2	400	1.4	0.5
030226	1.986	0.001	97	20	-0.89	0.2	-2.30	0.265	5.61	0.65	2	400	1.04	0.12
030328	1.52	0.001602	126.3	13.5	-1.14	0.03	-2.09	0.3	37.0	1.4	2	400	0.8	0.1
030329	0.1685	0.000004	67.9	2.2	-1.26	0.015	-2.28	0.055	163	10	2	400	0.5	0.1
030429	2.6564	0.0008	35	9	-1.1	0.25	-2.30	0.265	0.85	0.14	2	400	1.77	1

The regression model or the Liang-Zhang relationship (Liang et al. 2005) is

$$\hat{E}_{\gamma,iso} = 10^{k_0} E_p'^{k_1} t_b'^{k_2} \tag{2.14}$$

where k_0, $k_1$and k_2 are free parameters.

Then the free parameters and dispersion of this relationship from observation is determined. For each set of cosmological parameter ($\widetilde{\Omega}$), k_0, $k_1$and k_2 are evaluated for the best fit through the least $\chi^2(\widetilde{\Omega})$ test:

$$\chi^2(\widetilde{\Omega}) = \sum_{i=1}^{N} \frac{[log\hat{E}_{\gamma.iso,i}(\widehat{\Omega}) - logE_{\gamma,iso,i}(\widehat{\Omega})]}{\sigma^2_{log\hat{E}_{\gamma,iso,i}(\widehat{\Omega})}} \tag{2.15}$$

N is the number of GRB's in the GRB sample, $log\hat{E}_{\gamma.iso,i}(\widehat{\Omega})$ and $\sigma^2_{log\hat{E}_{\gamma,iso,i}(\widehat{\Omega})}$ are derived from the Liang-Zhang relationship

$$\sigma_{log\hat{E}_{\gamma,iso,i}} = \left[\left(k_1 \frac{\sigma_{E'_{p,i}}}{E'_{p,i}}\right)^2 + \left(k_2 \frac{\sigma_{t'_{b,i}}}{t'_{b,i}}\right)^2\right]^{1/2} \Big/ log10 \tag{2.16}$$

and $logE_{\gamma,iso,i}(\widehat{\Omega})$ is calculated from the observation

$$E_{\gamma,iso,i}(\widehat{\Omega}) = \frac{4\pi D_{L,i}^2(\widetilde{\Omega}) S_{\gamma,i} k_i}{1+z_i} \tag{2.17}$$

$D_{L,i}$ is luminosity distance, $S_{\gamma,i}$ is the observed fluence that is energy per unit of area detected by BAT, k_i is k-correction and z_i is redshift.

In the next section, it is shown that the Liang-Zhang relation can be considered as luminosity indicator. Next, it is discussed how I use a joint probability to compute the probability for a cosmology set, Ω. Here, I use the approach introduced in Liang et al. (2005):

1.The probability that the Liang-Zhang relationship can serve as luminosity indicator for a given cosmology, $\widetilde{\Omega}$ is

$$P_1(\widetilde{\Omega}) \propto e^{-\chi_1^2(\widetilde{\Omega})/2} \tag{2.18}$$

where

$$\chi_1^2(\widetilde{\Omega}) = \sum_{i=1}^{N} \frac{[log\hat{E}_{\gamma,iso,i}(\widetilde{\Omega}) - logE_{\gamma,iso,i}(\widetilde{\Omega})]}{\sigma^2_{log\hat{E}_{\gamma,iso,i}(\widetilde{\Omega})}} \tag{2.19}$$

$log\hat{E}_{\gamma,iso,i}(\widetilde{\Omega})$ and $\sigma^2_{log\hat{E}_{\gamma,iso,i}(\widetilde{\Omega})}$ are evaluated with k_0, k_1 an k_2 for the best fit from the empirical relation and $logE_{\gamma,iso,i}(\widetilde{\Omega})$ comes from the observation.

2.The probability for parameter set Ω according to the luminosity indicator derived for $\widetilde{\Omega}$ is

$$P_2(\Omega, \widetilde{\Omega}) \propto e^{-\chi_2^2(\widetilde{\Omega})/2} \tag{2.20}$$

where

$$\chi_2^2\left(\Omega,\widetilde{\Omega}\right)=\sum_{i=1}^{N}\frac{\left[\hat{\mu}_i(\widetilde{\Omega})-\mu_i(\Omega)\right]}{\sigma^2_{log\tilde{E}_{\gamma,iso,i}(\widetilde{\Omega})}} \tag{2.21}$$

$$\hat{\mu}_i=2.5\left[\hat{k}_0+\hat{k}_1 log E'_{p,i}+\hat{k}_2 log t'_{b,i}-log\left(4\pi S_{\gamma,i}k_i\right)+log(1+z_i)\right]-97.45 \tag{2.22}$$

$$\mu_i=log\left(D_{L,i}/10pc\right) \tag{2.23}$$

$$\sigma_{\hat{\mu}_i}=\frac{2.5}{ln10}\left[\left(k_1\frac{\sigma_{E'_{p,i}}}{E'_{p,i}}\right)^2+\left(k_2\frac{\sigma_{t'_{b,i}}}{t'_{b,i}}\right)^2+\left(\frac{\sigma_{S_{\gamma,i}}}{S_{\gamma,i}}\right)^2+\left(\frac{\sigma_{k_i}}{k_i}\right)^2+\left(\frac{\sigma_{z_i}}{1+z_i}\right)^2\right]^{1/2} \tag{2.24}$$

These two probabilities are independent; so, the joint probability is found via

$$P\left(\Omega,\widetilde{\Omega}\right)\propto P_1\left(\widetilde{\Omega}\right)P_2\left(\Omega,\widetilde{\Omega}\right) \tag{2.25}$$

$P\left(\Omega,\widetilde{\Omega}\right)$'s are mutually exclusive (they cannot happen at the same time); therefore, the final probability of a cosmology with the parameter set Ω is computed through summing over $\widetilde{\Omega}$'s

$$P(\Omega)\propto\sum_{\widetilde{\Omega}}P\left(\Omega,\widetilde{\Omega}\right) \tag{2.26}$$

The normalization factor of the probabilities is not shown. The result for the most probable model for each cosmology is shown in the next section.

2.3. Discussion

In the previous section, to search for a possible empirical relation and find the regression model parameters, a multivariable regression analysis is performed. The result of the regression analysis is shown in table 2.2. For four specific

cosmologies, the goodness of the best fit is represented by the correlation coefficient and significance from Spearman rank correlation analysis.

Table 2.2. Result of regression analysis

Parameter	$\kappa = -1$ $\Omega_M = 0.34, \Omega_\Lambda = 0.06$	Flat $\Omega_M = 0.23, \Omega_\Lambda = 0.77$	$\kappa = -1$ $\Omega_M = 0.26, \Omega_{r_c} = 0.08$	$Flat$ $\Omega_M = 0.18, \Omega_{r_c} = 0.17$
κ_0	47.99	47.90	47.96	47.90
κ_1	1.91	2.01	1.94	1.99
κ_2	-1.42	-1.42	-1.42	-1.43
Rank Correlation	0.9393	0.9393	0.9393	0.9393
Significance	2.09e-007	2.09e-7	2.09e-7	2.09e-7

The correlation coefficient shows how well the relation describes the relationship between observables and significance represents the likelihood of the correlation occurring by chance. In my evaluation, a correlation coefficient between 0.55 and 1 is considered an acceptable positive correlation and significance less than 0.001 is satisfactory. Based on the suggested criteria, for all four cosmologies positive correlation is concluded. In Fig 2.1 and 2.2, it is shown that $log\hat{E}_{\gamma.iso}$ and $logE_{\gamma,iso}$ have positive correlation for these four cosmologies.Therefore the Liang-Zhang relationship can be regarded as a luminosity indicator.

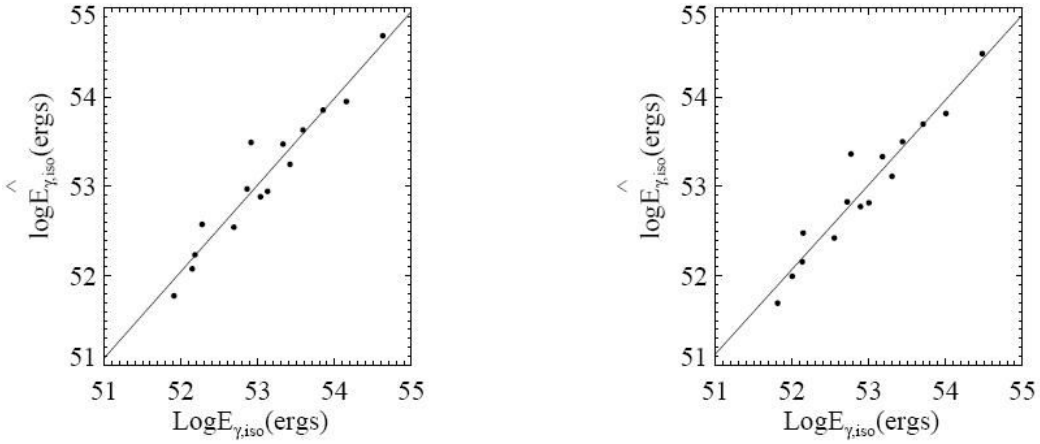

Figure 2.1. Plot of $\log E_{iso}$ derived from empirical relation versus calculated from observation for ΛCDM standard cosmology. *Left graph* shows the case where a flat universe is assumed and Ω_m and Ω_Λ are 0.23 and 0.77 respectively. *Right graph* shows the case where $\Omega_m = 0.34$, $\Omega_\Lambda = 0.06$ and $k = -1$.

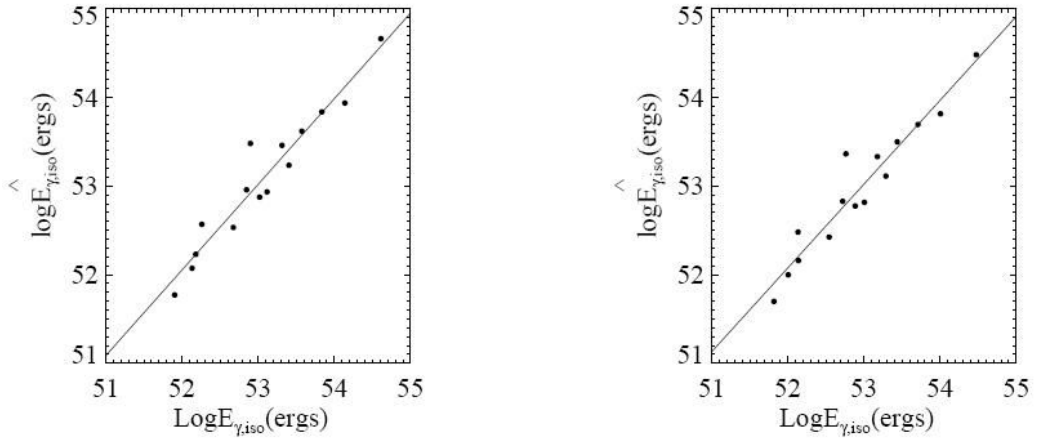

Figure 2.2. Plot of $\log E_{iso}$ derived from empirical relation versus calculated from observation for brane-induced gravity cosmology. *Left graph* shows the case where a flat universe is assumed and Ω_m and Ω_{r_c} are 0.18 and 0.17 respectively. *Right graph* shows the case where $\Omega_m = 0.26$, $\Omega_{r_c} = 0.08$ and $k = -1$.

Table 2.3 and 2.4 present the result for the most probable model for each cosmological model following the formalism outlined in the previous section. Table 2.3 shows the result when the curvature of the universe is assumed zero and table 2.4 is the result for the case when no assumption for curvature is considered.

Table 2.3. The most probable cosmology model with flat unverse assumption

Cosmological model	Ω_M	Ω_Λ or Ω_{r_c}	reduced χ^2
ΛCDM	0.23	0.77	0.32
Brane-induced gravity	0.18	0.17	0.32

Table 2.4. The most probable cosmology model with no assumption for curvature

Cosmological model	κ	Ω_M	Ω_Λ or Ω_{r_c}	reduced χ^2
ΛCDM	-1	0.34	0.06	0.33
Brane-induced gravity	-1	0.26	0.08	0.33

Figure 2.3 and 2.4 show the probability for each possible set of cosmology for ΛCDM and bran-induced gravity model respectively.

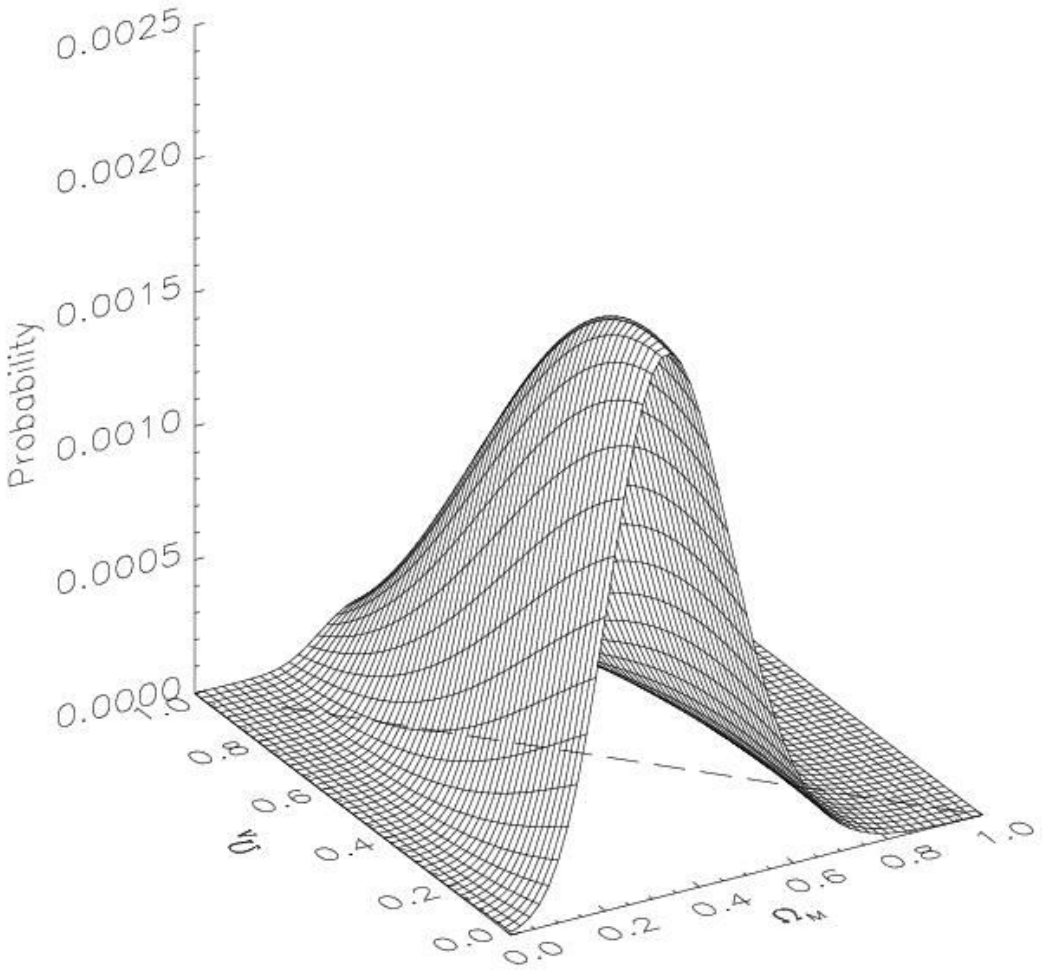

Figure 2.3. Probability for ΛCDM standard cosmology.

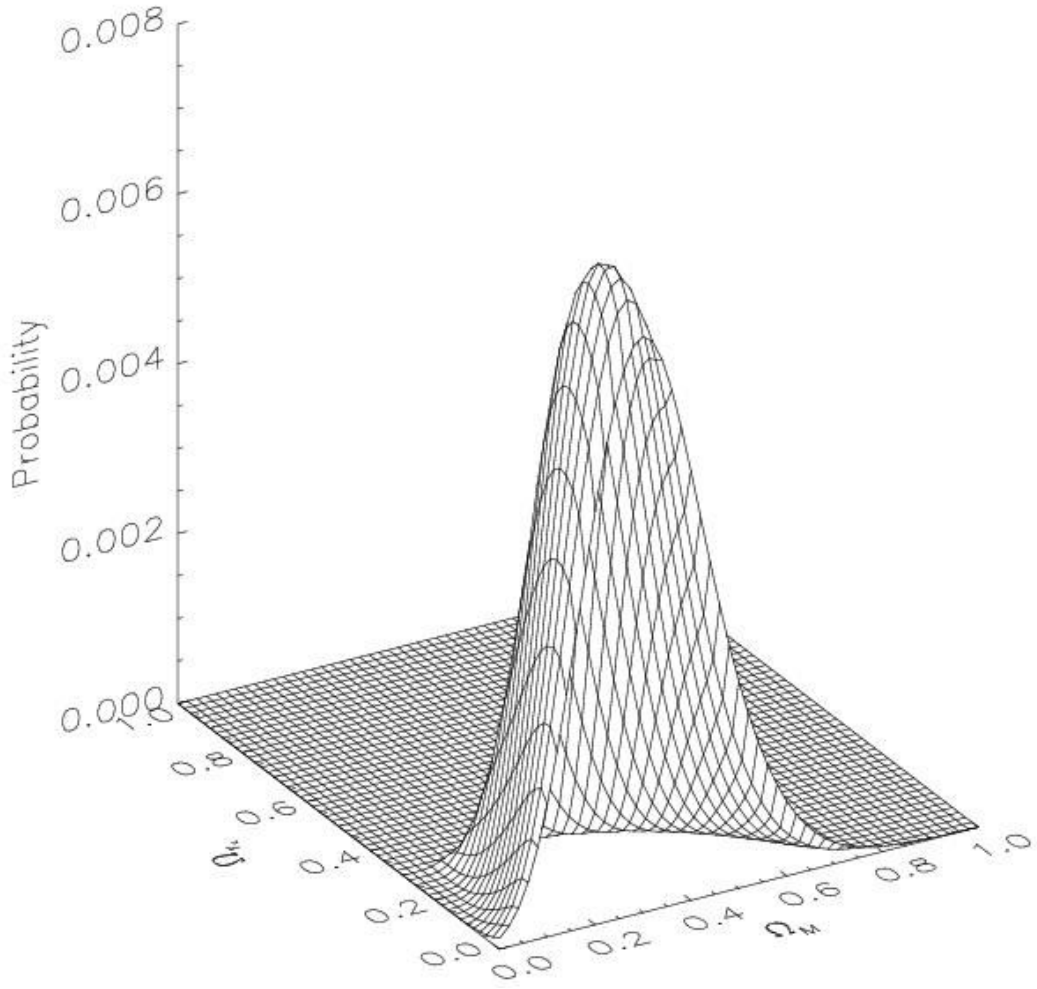

Figure 2.4. Probability for brane-induced gravity cosmology.

Figure 2.5 and 2.6 show the contours of liklihood for ΛCDM and brane-induced gravity model respectively.

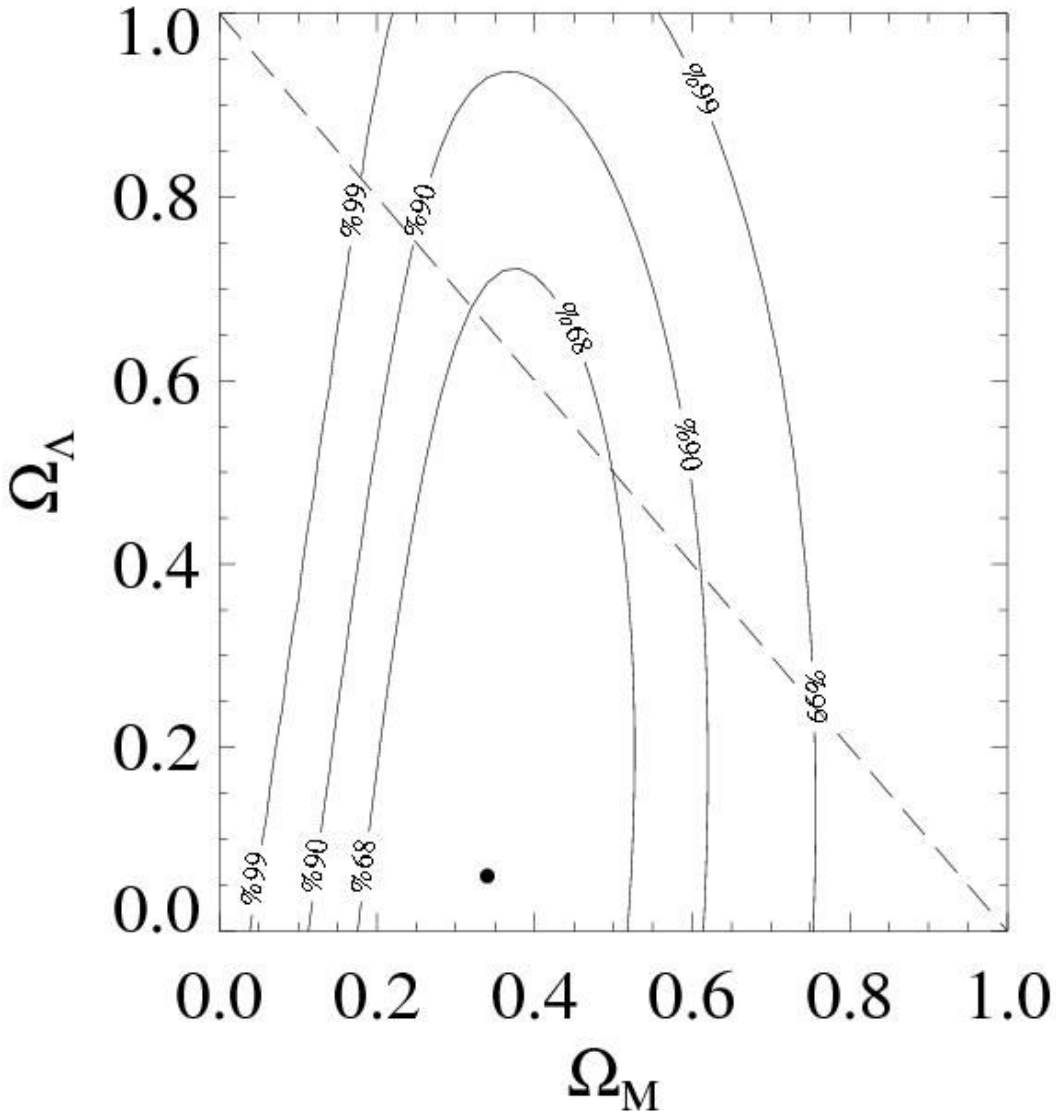

Figure 2.5. Countours of liklihood for ΛCDM standard cosmology

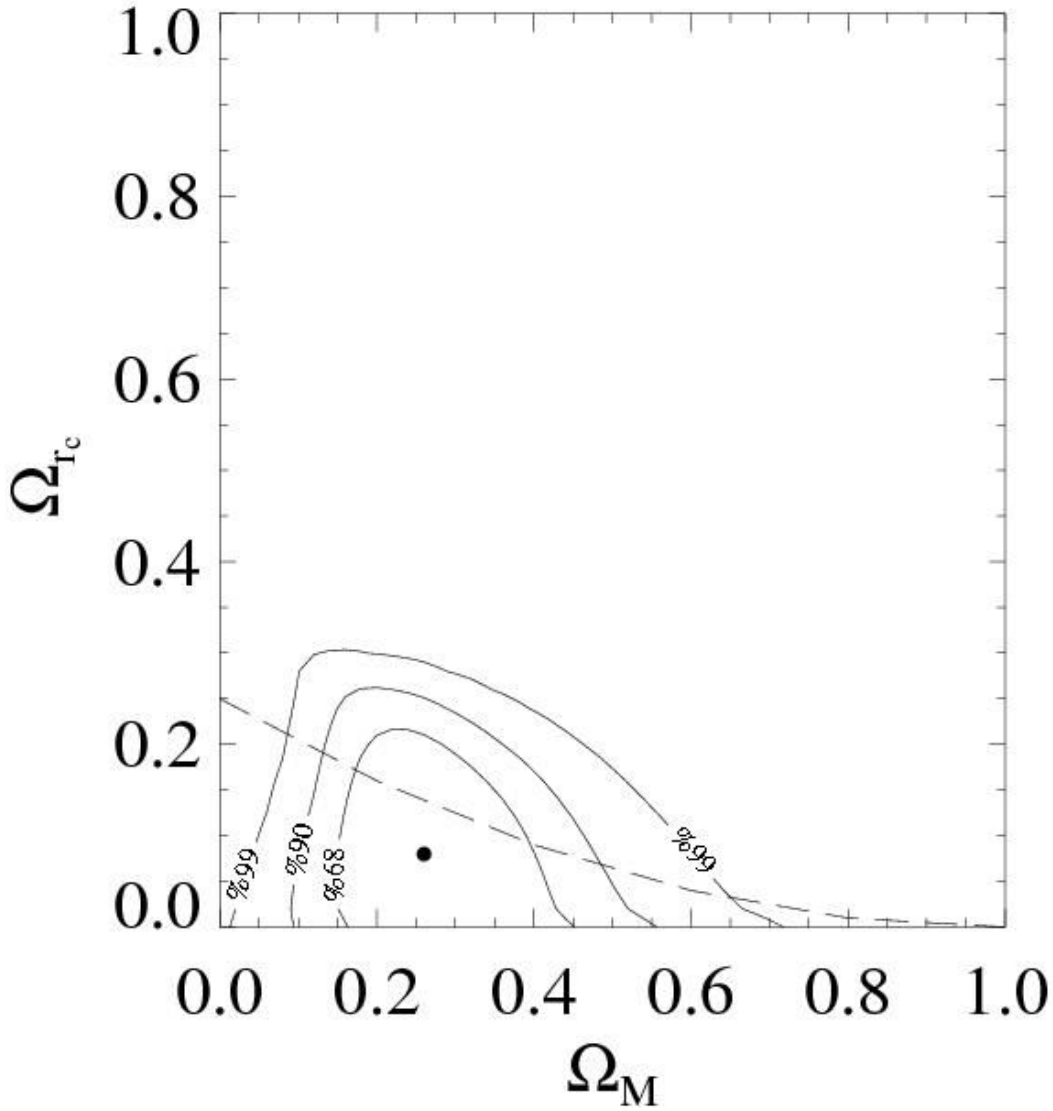

Figure 2.6. Countours of liklihood for brane-induced gravity cosmology

Figure 2.7 is the graph of distance modulus versus redshift. In this graph, solid line and dashed line show the Hubble diagram for the most probable model of ΛCDM and brane-induced gravity models when curvature of zero assumed.

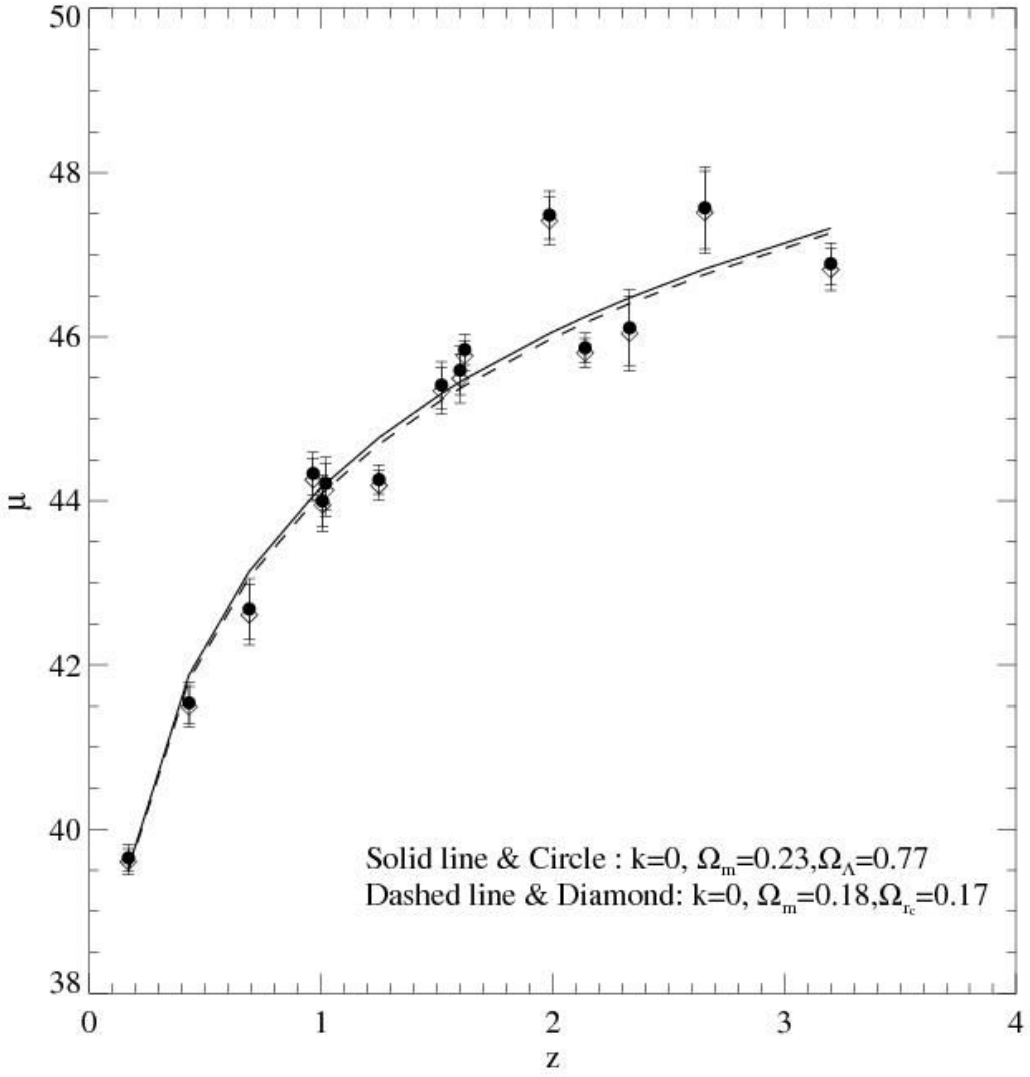

Figure 2.7. Hubble diagram for the most probable models with flat assumption for curvature.

The circle and dimond show the observation for former and latter cosmology. This diagram shows that the error bars are large in comparison to the difference between the two models and these two models are too close to be differentiated.

2.4. Conclusion and Prospect for This Work

For both cosmologies, the results for the flat universe is comparable with Deffayet et al. (2002) results from SNIa observation. Comparing contours of liklihood from GRB observations with figure 2.8 (countours of liklihood from WMAP and WMAP+HST), it is apparent that with improvement in using GRB for cosmography it might be possible to tighten the most probable model. This is due to the vertical direction of countours of liklihood from GRB observation.

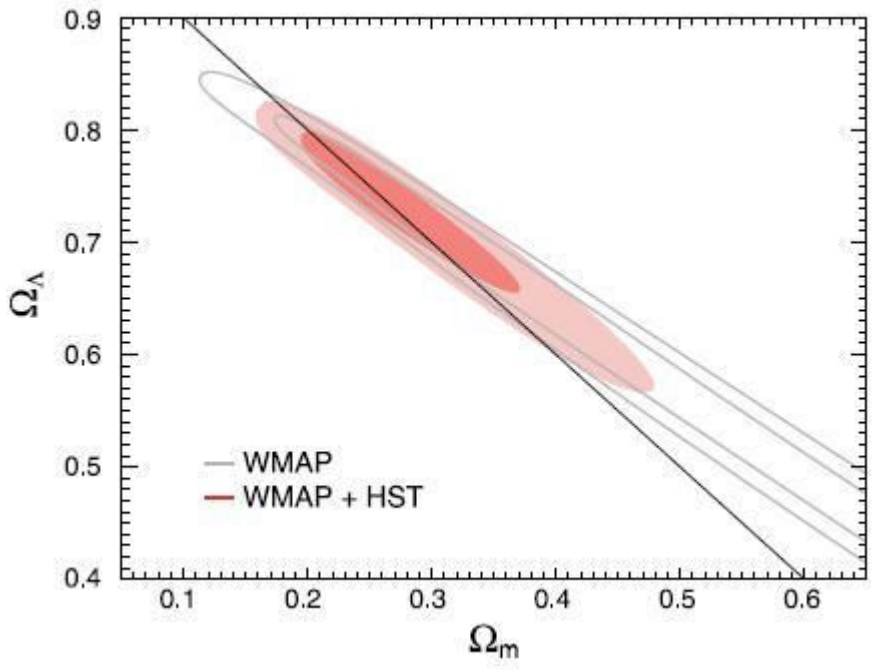

Figure 2.8. Countours of liklihood from WMAP and WMAP+HST. (Spergel et al. 2007)

Figure 2.9 shows distance modulus versus redshift for different cosmological models. This graph shows that all different models follow each other closely.

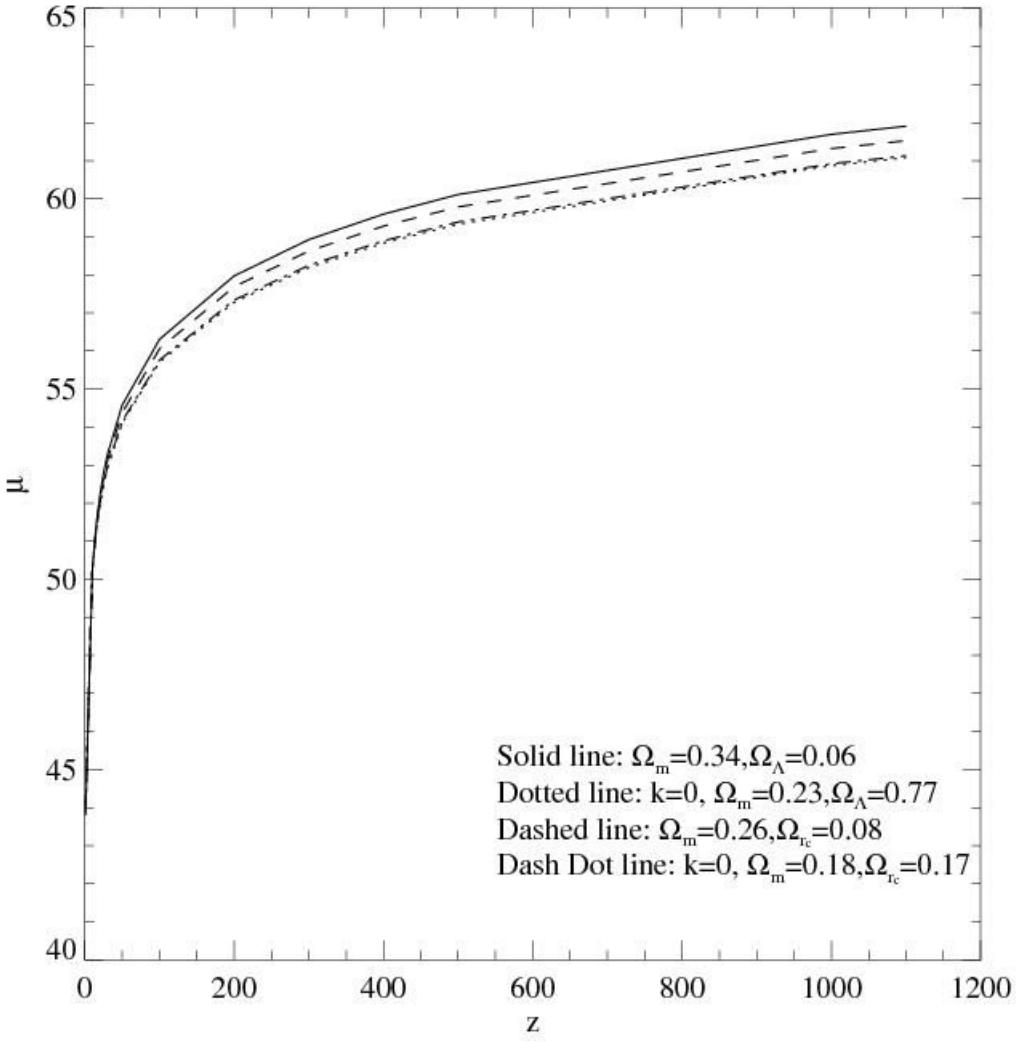

Figure 2.9. Hubble diagram for a wide range of redshift.

Lamb et al. (2000) shows that GRBs may be visible to z~20. Therefore, I regenerate the previous graph for this range of redshift (Figure 2.10).

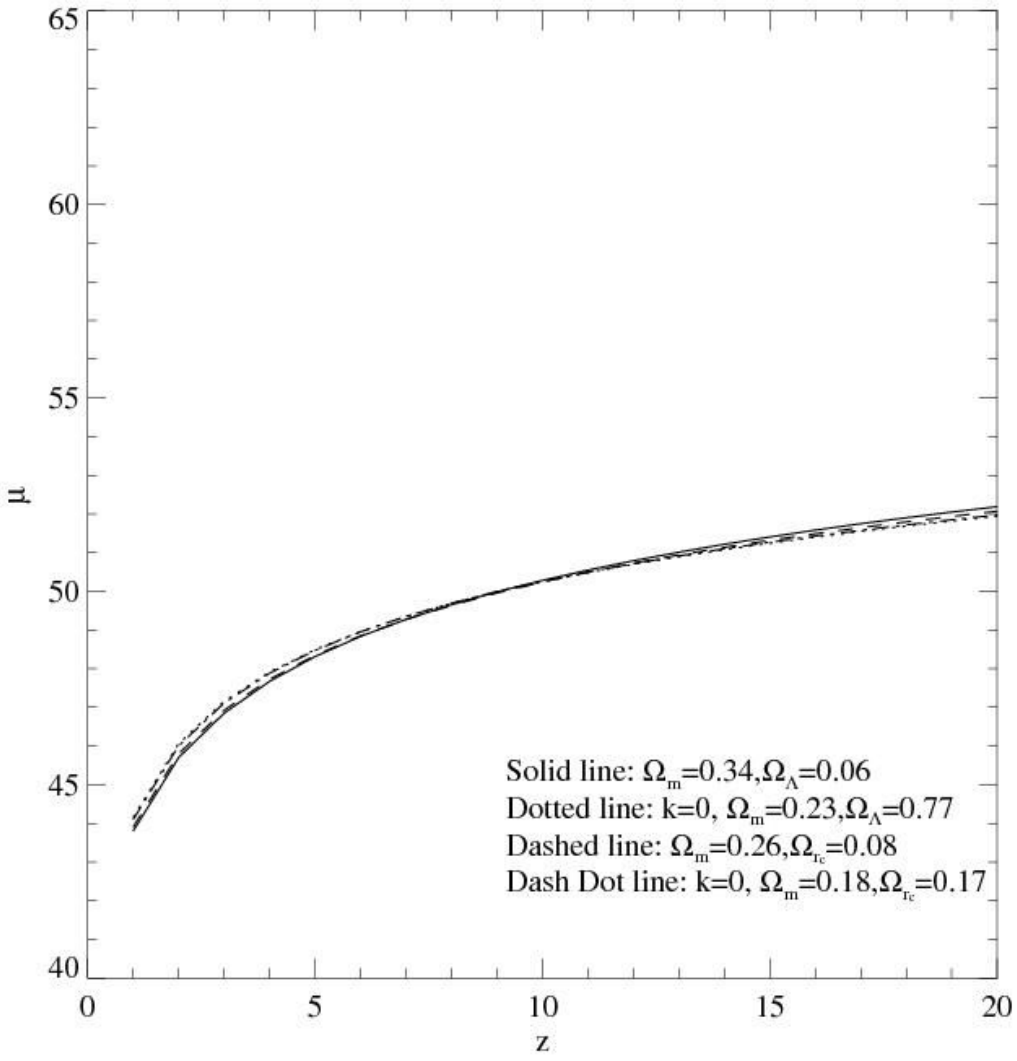

Figure 2.10. Hubble diagram for redshift range of 0-20.

To study this range of redshift more closely, the graph of distance modulus difference between each pair of discussed models versus redshift is produced.

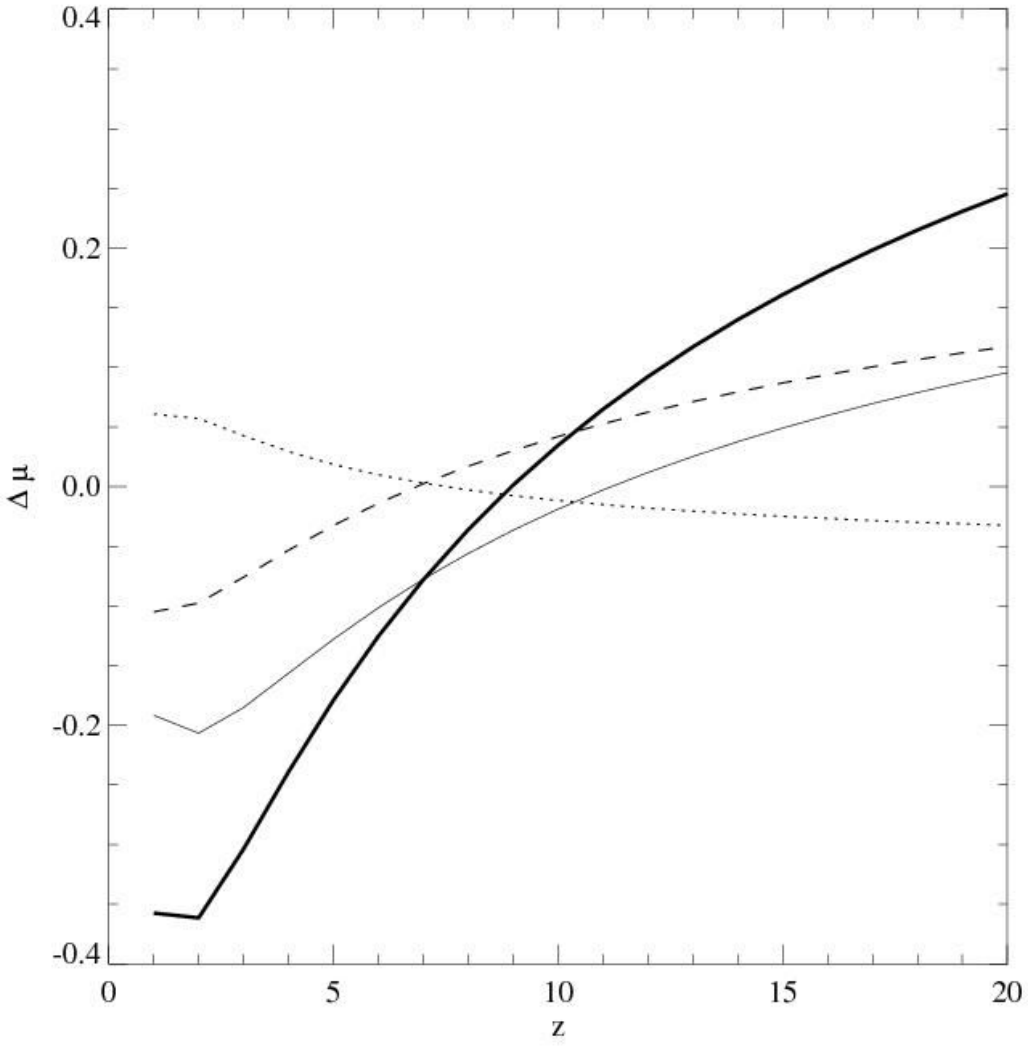

Figure 2.11. Distance modulus difference between each pair of dissussed for redshift range of 0-20.

The follwing is the description of each line in figure 2.11 and 2.12 which comes later. The solid dark line is from the difference of the two ΛCDM models. The solid light line is from the difference of the two brane-induced gravity model. The dashed line is from the difference of the two cosmological models with no assumption for curvature. The dotted line is from the difference of the two flat models. Figure 2.12 shows the same plot in figure 2.11 over a wider range of redshift.

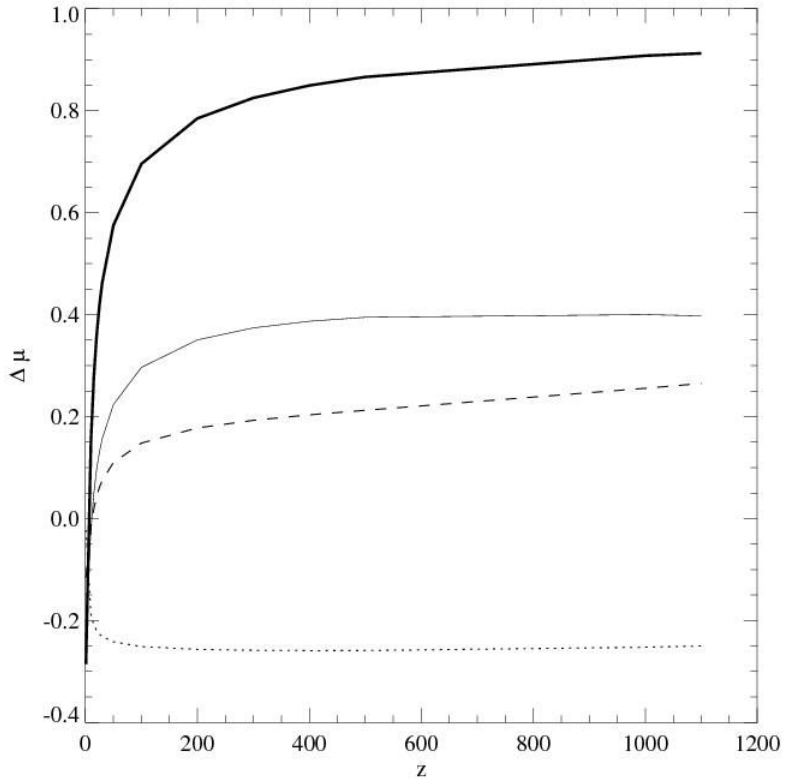

Figure 2.12. Distance modulus difference between each pair of discussed for a wide range of redshift.

Currently, the average error for distance modulus is 0.271 with standard deviation of 0.0973. With this precision the error for distance modulus is comparable with the difference between two flat models for redshift greater than 10 but not with the difference between the two models with no assumption for curvature over any range of redshift less than 20. For the other two differences, there is a turning point in the middle which makes the lower and higher redshift GRBs more critical to differentiate the models.

Expanding the sample and including more high and low redshift GRBs help to improve the result. Another element to create a large sample of GRBs for this study is to measure break time for GRBs that requires early infrared observation.

Chapter 3

CORRELATIONS AND EVOLUTION OF GRB PROPERTIES

A Gamma-ray burst output consists of its prompt emission and its afterglow. Here the GRB's prompt emission and shallow decay of its x-ray afterglow are used to explore any correlation among prompt emission and afterglow properties as well as possible GRB property evolution.

3.1 Introduction

Gamma-ray bursts are electromagnetic signals. They were first discovered in the late 1960s (Klebesadel et al. 1973; Mazets et al. 1974). Prompt emission and afterglow are the two components of a gamma-ray burst output. Prompt emission happens in γ-ray band at sub Mev energies and lasts only tens of seconds. Afterglows are broad-band, having been detected in the x-ray, the optical/infrared and the radio bands. X-ray afterglows are the most commonly detected and last on average for about 10^5seconds.

Looking into correlation and evolution of GRB prompt emission and afterglow has many advantages. It helps to open windows to comprehend the physics of GRBs and examine different GRB models. It is also possible to use GRB correlation as an accurate redshift estimator and more importantly to constrain the cosmological parameters. XRT flares of GRB afterglow are thought to be the result of central engine activity. Studying this component leads us to understand GRB flare and central engine nature.

3.2 Swift XRT data analysis

My sample includes 28 GRBs observed by Swift. The data is taken from Swift GRB detection archive by BAT and XRT as of October 11 (Table 3.1).

Table 3.1. Swift GRB sample

GRB	T_{90} (sec)	S_γ (10^{-7}ergs cm^{-2})	σ_S (10^{-7}ergs cm^{-2})	Γ	NH ($10^{21} cm^{-2}$)	z	$t_{iNormal}$ (sec)	$t_{fShallow}$ (sec)
(1)	(2)	(3)	(4)	(5)	(6)	(7)	(8)	(9)
050416A	2.5	3.67	0.37	2.02	2.5	0.6535	100	300000
050730	156.5	23.8	1.52	1.8	1	3.97	3000	200000
050802	19	20	1.57	1.9	0.66	1.71	300	100000
050803	87.9	21.5	1.35	1.8	1.98	0.422	400	400000
051016B	4	1.7	0.22	6.2	4.8	0.9364	100	100000
060108	14.3	3.69	0.37	1.76	0.17	2.03	450	200000
060124	750	4.61	0.53	1.40	1.72	2.30	10000	1000000
060206	7.6	8.31	0.42	2	0.4	4.045	100	1000000
060210	255	76.6	4.09	1.93	16.4	3.91	3000	1000000
060614	108.7	204	3.63	1.65	1.3	0.13	2000	1000000
060607A	102.2	25.5	1.12	1.64	7.9	3.082	300	100000
060708	10.2	4.94	0.37	3.3	1.5	2.3	4000	500000
060714	115	28.3	1.67	1.97	1.89	2.71	300	100000
060729	115.3	26.1	2.11	2.14	1	0.54	350	2000000
060814	145.3	146	2.39	1.67	2.7	0.84	400	100000
061121	81.3	137	1.99	2.25	2.3	1.314	200	300000
070306	209.5	53.8	2.86	2.29	3.9	1.497	300	1000000
070508	20.9	196	2.73	2.05	3.8	0.82	100	200000
070521	37.9	80.1	1.77	2.11	7	0.553	300	50000
080411	56	264	1	2.14	1.5	1.03	4000	2000000
080413B	8.0	32	1	2.05	3.2	1.10	500	800000
080430	16.2	12	1	2.42	0.46	0.759	200	2000000
080516	5.8	2.6	0.4	2.7	13	3.2	100	50000
080810	106	46	2	1.98	0.328	3.35	300	100000
080905B	128	18	2	1.49	13.2	2.374	200	400000
081007	10	7.1	0.8	3	6.6	0.5295	200	1000000
081029	270	21	2	1.9	0.27	3.847	2000	100000
090102	27	0.68	0.03	1.8	7	1.548	600	200000

The data is shown in table 3.1 with the following heading: (1) GRB name; (2) BAT T_{90}; (3) γ-ray fluence; (4) γ-ray fluence error; (5) low-energy spectral index; (6) low-energy spectral index error; (7) redshift; (8) start time of normal segment; (9) end time of shallow segment. This sample is selected out of 65 GRBs. The sample only includes the redshift-known GRBs that have a well-defined XRT lightcurve and feature both shallow and normal decay in their x-ray afterglow light curves. Shallow and normal decay are two of the five Gamma-Ray Burst XRT light curve segments (Zhang et al. 2006) . These segments have typical slopes of -0.5 and -1.2 respectively. The time where shallow and normal segment meet is called break time. Break time is stated in GRB rest frame throughout this paper. Another component of Gamma-Ray Burst XRT light curve, appearing in roughly 50% of GRBs, is called flare. Seven GRBs of our sample contain one or more flares.

The reduced data for X-ray afterglow light curve of each GRB is taken from Swift Data Product of UNLV GRB group (http://grb.physics.unlv.edu/~xrt/xrtweb/web/sum.html). In this section, the fit function for XRT light curves and their flares are introduced.

To study XRT light curve and extract different GRB properties, the light curve is fitted with a smooth broken power-law:

$$L = L_0\left((x_b t)^{\alpha\omega} + (x_b t)^{\beta\omega}\right)^{-1/\omega} \tag{3.1}$$

where

$$x_b = \frac{1}{t_b} \tag{3.2}$$

t_b is the break time between shallow and normal decay segments and ω describes sharpness of the break that is taken to be one here. L_0 , α and β are other fitting parameters. Table 3.2 contains smooth broken power-law fitting parameters for XRT light curve of each GRB and their errors. Table 3.2 also reports the $\chi^2$of each fit. Figure 3.1 displays the fit for each light curve.

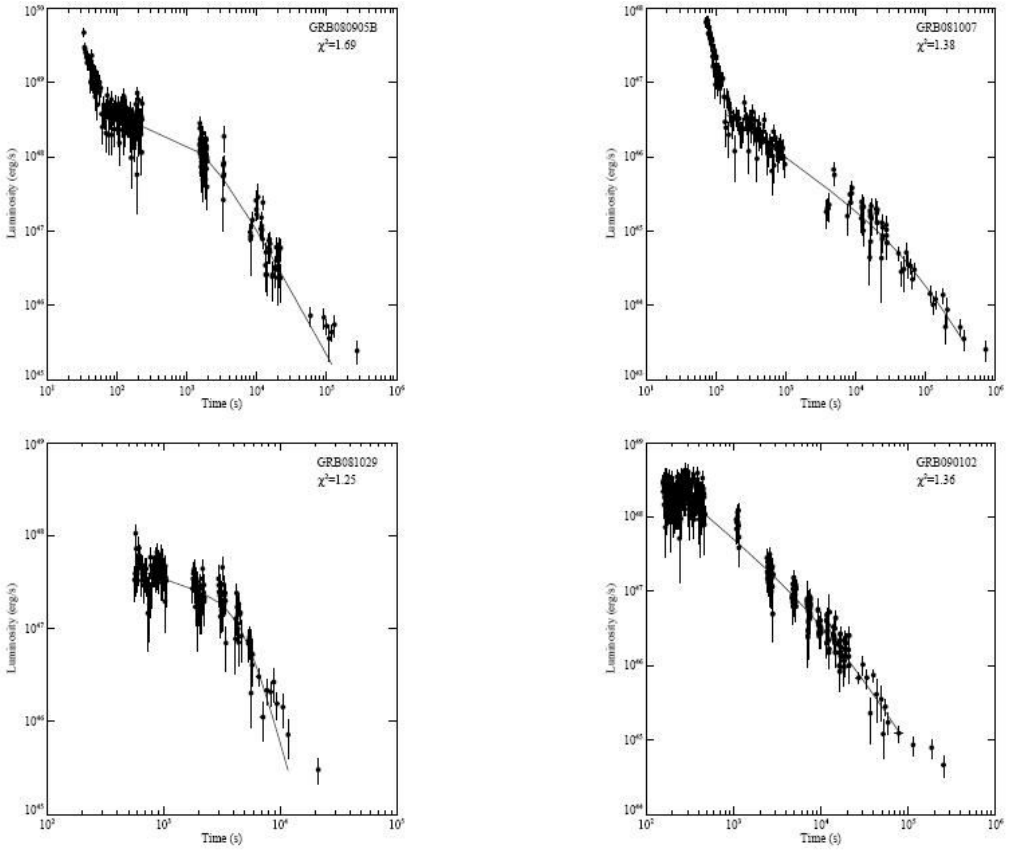

Figure 3.1. Smooth broken power-law fit for GRB XRT lightcurves

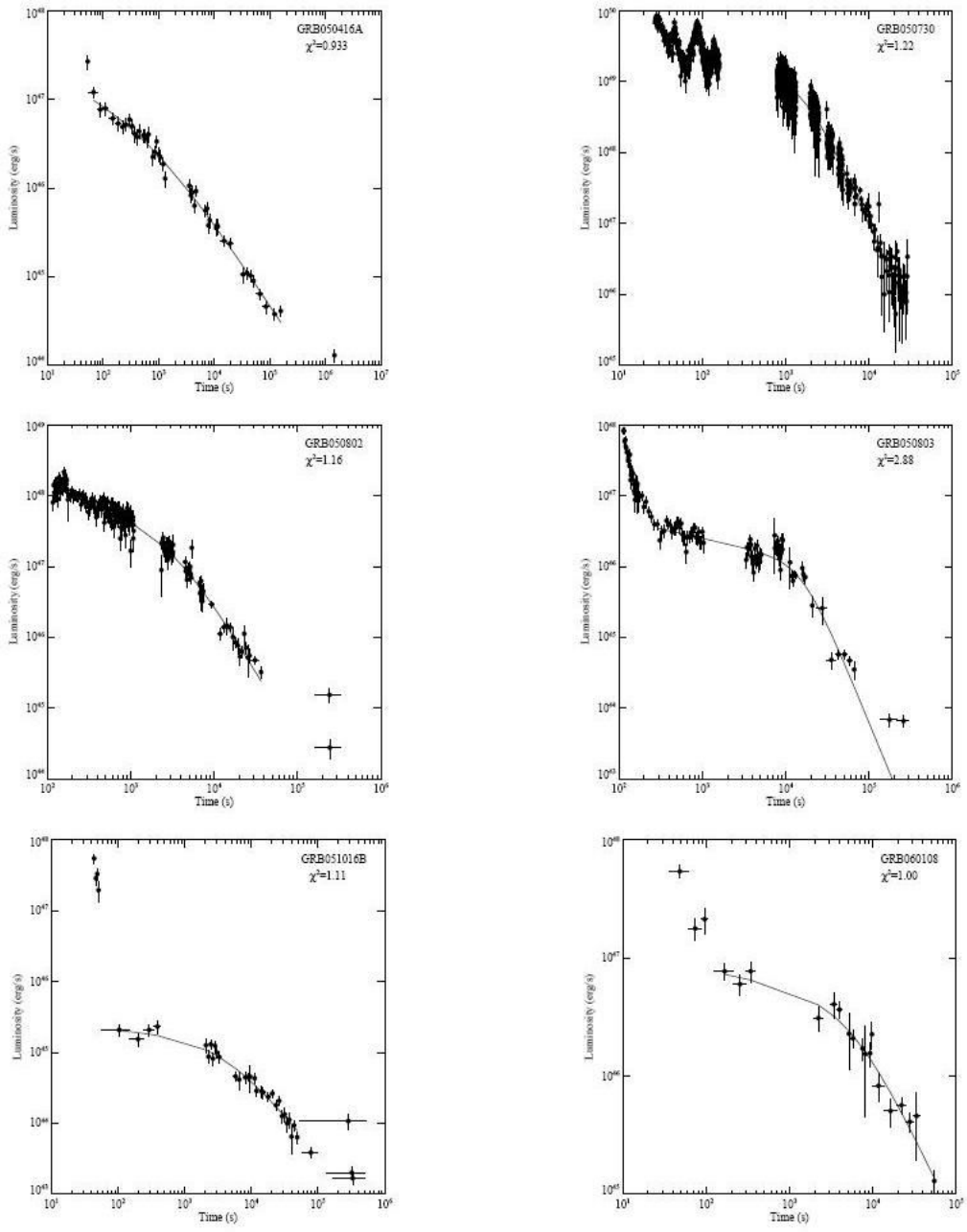

Figure 3.1. Continued.

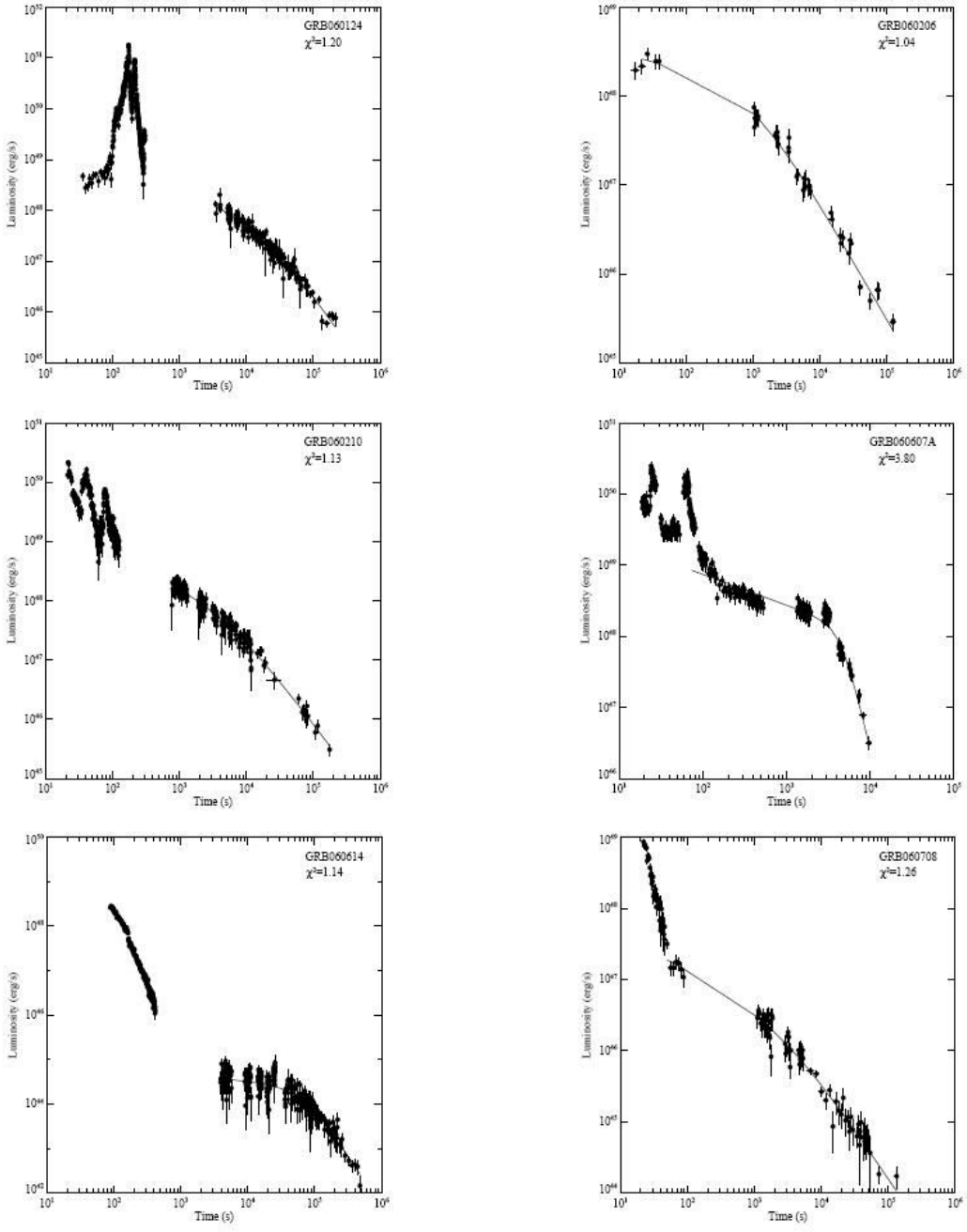

Figure 3.1. Continued.

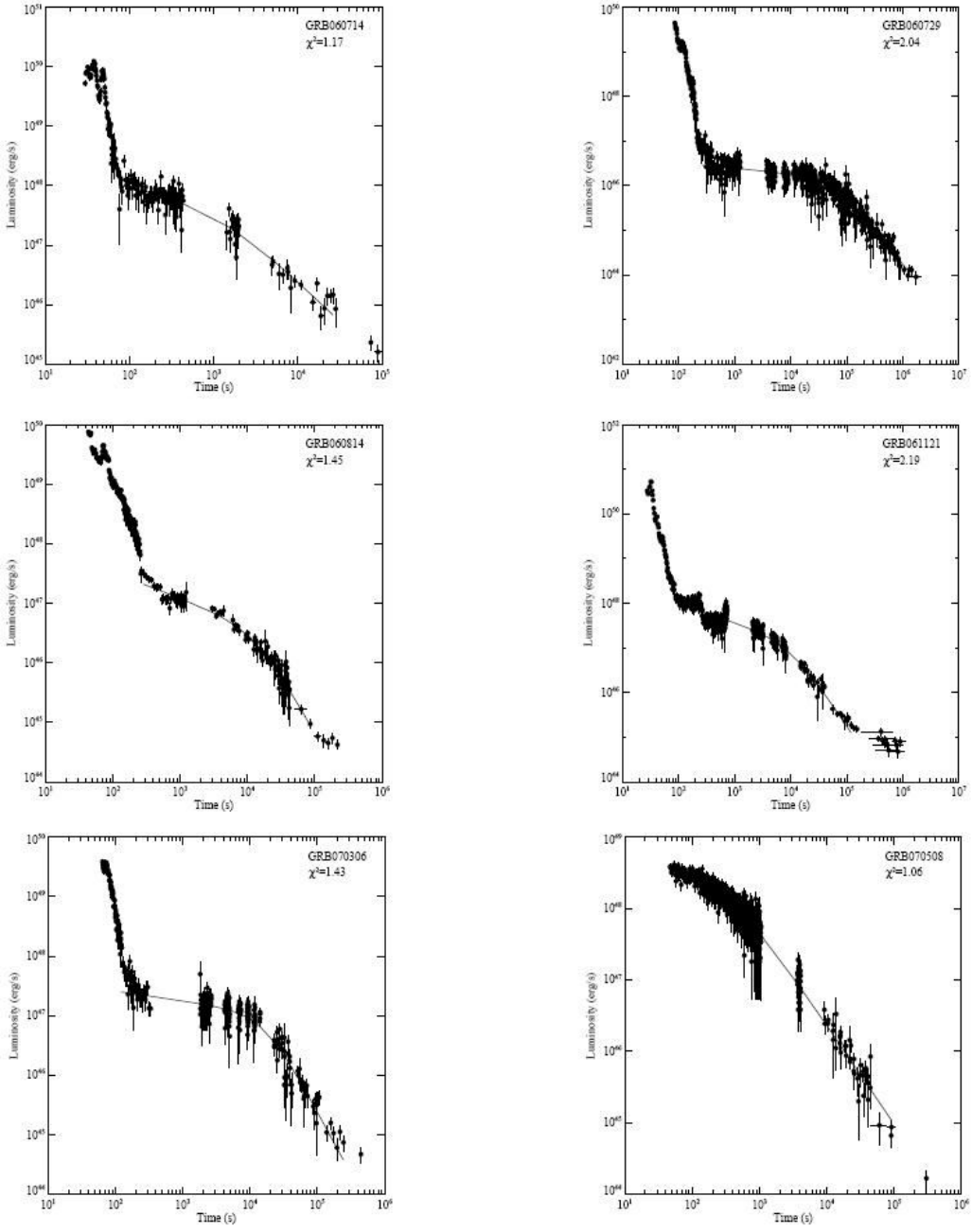

Figure 3.1. Continued.

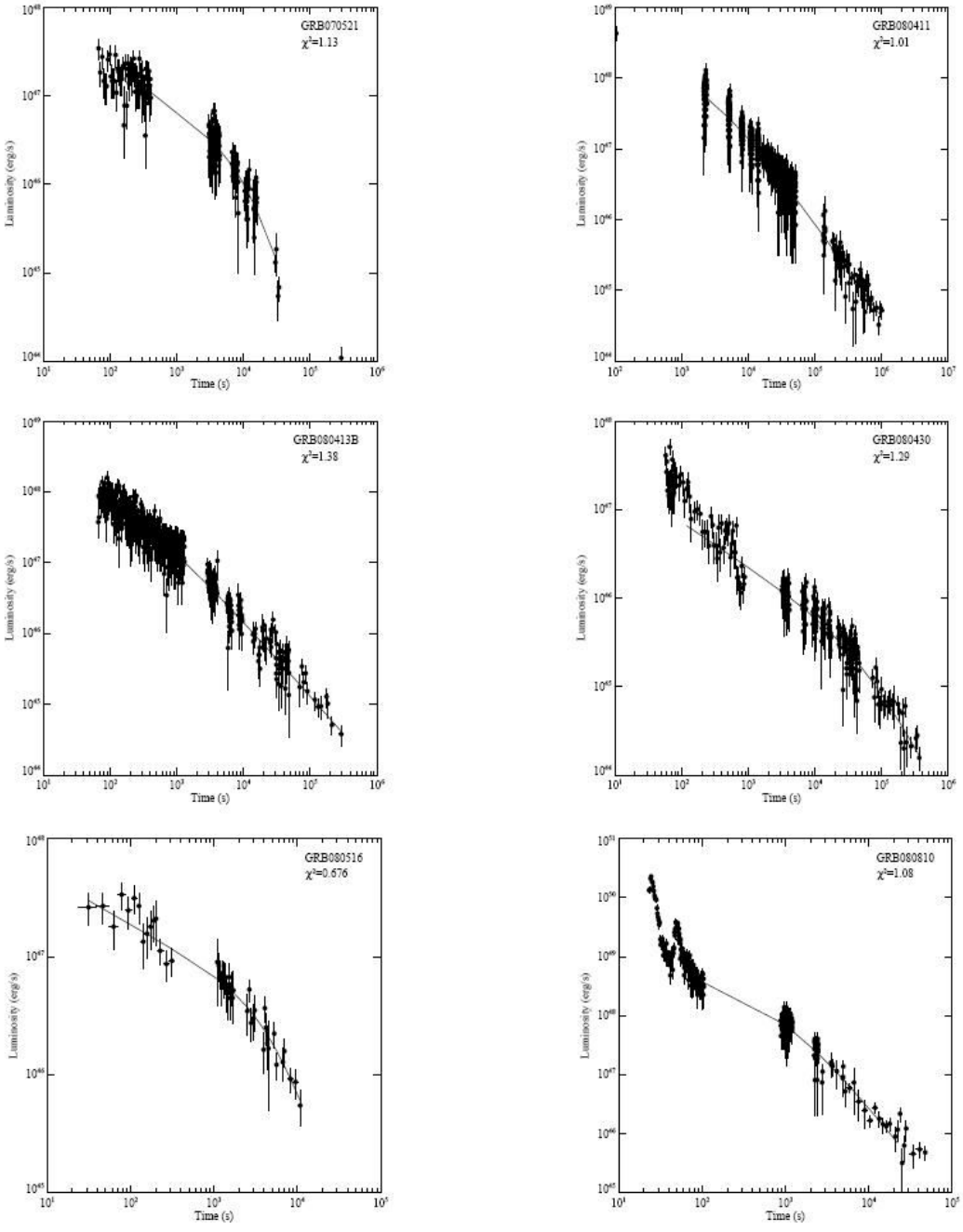

Figure 3.1. Continued.

Table 3.2. Smooth broken power-law fitting parameters for XRT light curves.

GRB	L_0 ($ergs\ sec^{-1}$)	σ_{L_0} ($ergs\ sec^{-1}$)	x_b (sec^{-1})	σ_{x_b} (sec^{-1})	α	σ_α	β	σ_β	χ^2
050416A	6.01E+46	4.78E+46	1.50E-03	1.83E-03	0.30	0.17	0.96	0.08	0.93
050730	1.01E+49	1.54E+48	5.83E-04	5.49E-05	0.32	0.16	2.63	0.06	1.22
050802	2.64E+47	4.36E+46	2.95E-04	4.19E-05	0.49	0.04	1.97	0.08	1.16
050803	1.20E+46	1.04E+45	6.28E-05	4.84E-06	0.26	0.03	2.86	0.15	2.88
051016B	1.59E+45	7.61E+44	2.69E-04	2.02E-04	0.07	0.14	1.14	0.16	1.11
060108	4.56E+46	2.41E+46	1.82E-04	1.16E-04	0.14	0.14	1.51	0.23	1.00
060124	2.61E+47	1.76E+47	3.38E-05	1.71E-05	0.76	0.13	1.95	0.16	1.20
060206	1.35E+48	4.52E+47	1.06E-03	4.23E-04	0.18	0.08	1.31	0.05	1.04
060210	8.94E+47	4.45E+47	2.18E-04	1.08E-04	0.49	0.12	1.51	0.09	1.13
060607A	1.43E+48	6.22E+46	2.22E-04	4.93E-06	0.43	0.01	5.02	0.21	3.80
060614	2.38E+44	3.11E+43	1.49E-05	1.65E-06	0.16	0.06	2.29	0.11	1.14
060708	4.60E+46	3.23E+46	6.81E-04	6.51E-04	0.13	0.93	1.33	0.17	1.27
060714	5.16E+47	2.89E+47	8.86E-04	6.03E-04	0.27	0.16	1.37	0.15	1.17
060729	1.53E+46	8.45E+44	1.81E-05	1.27E-06	0.12	0.02	1.54	0.03	2.06
060814	1.99E+46	2.55E+45	4.29E-05	3.89E-06	0.59	0.02	2.72	0.27	3.93
061121	1.46E+47	1.32E+46	9.90E-05	8.81E-06	0.41	0.02	1.91	0.06	2.19
070306	1.12E+47	8.69E+45	6.12E-05	5.21E-06	0.17	0.03	2.10	0.08	1.43
070508	2.64E+48	3.32E+47	3.04E-03	4.64E-04	0.21	0.06	1.39	0.02	1.06
070521	1.70E+46	4.30E+45	8.78E-05	1.72E-05	0.56	0.04	2.33	0.31	1.13
080411	7.34E+47	2.61E+47	2.73E-04	1.08E-04	0.41	0.18	1.33	0.04	1.01
080413B	6.21E+47	1.71E+47	3.33E-03	1.53E-03	0.13	0.32	1.07	0.05	1.38
080430	3.06E+45	1.39E+45	1.86E-05	9.23E-06	0.50	0.05	1.44	0.16	1.29
080516	3.90E+46	1.81E+46	2.09E-04	9.03E-05	0.40	0.08	2.00	0.56	0.68
080810	1.01E+48	5.91E+47	7.67E-04	3.97E-04	0.52	0.11	1.74	0.15	1.08
080905B	1.99E+48	4.70E+47	5.60E-04	1.43E-04	0.15	0.08	1.69	0.09	1.69
081007	6.03E+44	3.82E+44	1.52E-05	8.96E-06	0.67	0.05	1.64	0.25	1.38
081029	1.79E+47	2.67E+46	2.11E-04	1.65E-05	4.52	0.56	0.42	0.08	1.25
090102	4.33E+46	3.36E+46	7.30E-05	4.00E-05	0.97	0.06	1.92	0.19	1.36

Using the fitting parameter from table 3.2, luminosity at break time is calculated

$$L_{t_b} = L_0\left((x_b t_b)^{\alpha\omega} + (x_b t_b)^{\beta\omega}\right)^{-1/\omega} \tag{3.3}$$

The results for L_{t_b} and its error are shown in table 3.3.

Table 3.3. GRB luminosity at break time

GRB	z	$T_{90RestFrame}$ (sec)	t_b (sec)	L at t_b (ergs sec^{-1})	σ_L at t_b (ergs sec^{-1})
(1)	(2)	(3)	(4)	(5)	(6)
050416A	0.65	1.51	666.28	3.01E+46	2.39E+46
050730	3.97	31.49	1716.05	5.04E+48	7.70E+47
050802	1.71	7.01	3394.60	1.32E+47	2.18E+46
050803	0.42	61.81	15929.81	6.02E+45	5.19E+44
051016B	0.94	2.07	3719.63	7.97E+44	3.80E+44
060108	2.03	4.72	5488.42	2.28E+46	1.21E+46
060124	2.30	227.27	29594.20	1.30E+47	8.80E+46
060206	4.05	1.51	939.30	6.74E+47	2.26E+47
060210	3.91	51.93	4594.24	4.47E+47	2.23E+47
060607A	3.08	25.04	4511.64	7.13E+47	3.11E+46
060614	0.13	96.37	67140.24	1.19E+44	1.56E+43
060708	2.30	3.09	2419.37	1.52E+46	9.99E+45
060714	2.71	31.00	1128.26	2.58E+47	1.44E+47
060729	0.54	74.87	53635.13	7.82E+45	4.32E+44
060814	0.84	78.97	14030.31	1.95E+46	3.13E+45
061121	1.31	35.13	10101.96	7.28E+46	6.58E+45
070306	1.50	83.90	16329.29	5.58E+46	4.35E+45
070508	0.82	11.48	329.12	1.32E+48	1.66E+47
070521	0.55	24.40	11385.51	8.49E+45	2.15E+45
080411	1.03	27.59	3510.06	3.81E+47	1.28E+47
080413B	1.10	3.81	283.56	3.50E+47	1.89E+47
080430	0.76	9.21	53861.44	1.53E+45	6.95E+44
080516	3.20	1.38	4790.37	1.95E+46	9.07E+45
080810	3.35	24.37	1303.52	5.05E+47	2.96E+47
080905B	2.37	37.94	1785.94	9.93E+47	2.35E+47
081007	0.53	6.54	65716.58	3.01E+44	1.91E+44
081029	3.85	55.70	4750.47	8.94E+46	1.33E+46
090102	1.55	10.60	13698.59	2.17E+46	1.68E+46

The data is shown in table 3.3 with the following heading: (1) GRB name; (2) redshift ; (3) T_{90} in the rest frame of the GRB; (4) break time; (5) luminosity at break time; (6) the error of luminosity at break time.

Another GRB property which is evaluated from XRT light curve is $E_{plateau}$. $E_{plateau}$ is the total energy emitted during the shallow decay (plateau). $E_{plateau}$ is calculated through

$$E_{plateau} = \int_{t_0}^{t_b} L(t)\, dt \tag{3.4}$$

where t_0 is the lower point of shallow segment and t_b is the upper point of shallow segment which is called break time. L(t) is luminosity. The results for $E_{plateau}$ and its error are shown in table 3.4. The data is shown in table 3.3 with the following heading: (1) GRB name; (2) redshift ; (3) T_{90} in the rest frame of the GRB; (4) $E_{plateau}$ for normal decay segment; (5) the error for $E_{plateau}$ for normal decay.

To investigate XRT flare properties, a Gaussian function is used as fitting function. μ, σ and A are the fitting parameters and represent the mean, standard deviation and total area of the Gaussian curve. Table 3.5 contains the fitting parameters of the fit along with the χ^2 for each flare fit. The data is shown in table 3.5 with the following heading: (1) GRB name; (2) the number of XRT flares visually detected on GRB light curve from left ; (3) constant; (4) mean of the fitted Gaussian curve ; (5) sigma of the fitted Gaussian curve; (6) the total area

of the fitted Gaussian curve; (7) χ^2. Figure 3.2 shows the Gaussian fit to the flares of XRT light curves.

Table 3.4. Afterglow plateau energy

GRB	z	$T_{90RestFrame}$ (sec)	$E_{plateau}$ (ergs)	$\sigma E_{plateau}$ (ergs)
(1)	(2)	(3)	(4)	(5)
050416A	0.65	1.51	2.96E+49	1.22E+48
050730	3.97	31.49	9.38E+51	1.61E+50
050802	1.71	7.01	1.15E+51	2.07E+49
050803	0.42	61.81	2.09E+50	5.11E+48
051016B	0.94	2.07	4.44E+48	4.61E+47
060108	2.03	4.72	2.06E+50	1.86E+49
060124	2.30	227.27	1.02E+52	1.71E+50
060206	4.05	1.51	1.07E+51	8.63E+49
060210	3.91	51.93	3.56E+51	5.83E+49
060607A	3.08	25.04	9.39E+51	1.51E+50
060614	0.13	96.37	1.47E+49	3.72E+47
060708	2.30	3.09	9.02E+49	4.81E+48
060714	2.71	31.00	4.82E+50	1.78E+49
060729	0.54	74.87	7.07E+50	9.63E+48
060814	0.84	78.97	6.97E+50	1.44E+49
061121	1.31	35.13	1.89E+51	2.62E+49
070306	1.50	83.90	1.72E+51	3.63E+49
070508	0.82	11.48	5.65E+50	7.19E+48
070521	0.553	24.40	3.09E+50	8.68E+48
080411	1.03	27.59	1.06E+51	3.73E+49
080413B	1.1	3.81	1.38E+50	3.73E+48
080430	0.759	9.21	2.42E+50	5.65E+48
080516	3.2	1.38	2.45E+50	1.31E+49
080810	3.35	24.37	1.58E+51	6.06E+49
080905B	2.374	37.94	2.98E+51	8.81E+49
081007	0.5295	6.54	8.46E+49	3.07E+48
081029	3.847	55.70	9.82E+50	3.20E+49
090102	1.548	10.60	1.85E+51	4.86E+49

Table 3.5 Gaussian fit parameters for GRB XRT flares

GRB	# of flare	constant (erg/sec)	μ (sec)	σ (sec)	area (ergs)	χ^2
(1)	(2)	(3)	(4)	(5)	(6)	(7)
050730	1	3.60E+49	46.49	-0.84	-6.41E+49	5.30
050730	2	1.61E+49	86.62	7.80	7.83E+50	9.99
050730	3	1.82E+49	138.05	3.26	1.26E+50	9.50
060124	1	2.31E+50	173.39	4.09	1.14E+52	21.31
060124	2	2.70E+50	213.69	3.69	5.56E+51	6.48
060607A	1	4.23E+49	25.32	1.38	5.13E+50	7.56
060607A	2	3.20E+49	63.84	4.05	1.16E+51	9.39
060714	1	4.07E+49	37.49	2.26	3.90E+50	4.86
060714	2	2.14E+49	47.94	1.84	3.05E+50	3.00
060729	1	1.04E+49	117.62	4.17	5.98E+49	5.12
060814	1	2.75E+49	72.15	2.13	9.59E+49	5.67
080810	1	1.07E+49	49.82	2.34	1.47E+50	6.99

To study the flares with respect to the underlying XRT light curve power-law, a "Ratio" is defined. If t_{max} is the time where flare's Gaussian fit is maximum, "Ratio" is defined as:

$$\text{Ratio} = \frac{L_{flare}(t_{max})}{L_{power-law}(t_{max})} \tag{3.5}$$

where $L_{flare}(t_{max})$ and $L_{power-law}(t_{max})$ are flare Gaussian fit at $t_{max}$and Underlying power-law fit at t_{max} respectively. The results for the ratio and corresponding luminosities are presented in table 3.6. The data is shown in table 3.5 with the following heading: (1) GRB name; (2) the number of XRT flares visually detected on GRB light curve from left ; (3) redshift; (4) T_{90} in the rest frame of the GRB ; (5) value of the flare Gaussian fit at the mean of the fitted Gaussian curve for the flare; (6) value of the underlying powerlaw at the mean of the fitted Gaussian curve for the flare; (7) Ratio of (5) over (6).

Table3.6 XRT flare and light curve comparison by "Ratio"

GRB	# of flare	Redshift	$T_{90RestFrame}$ (sec)	L_{Flare} (erg/sec)	$L_{UnderlyingLightcurve}$ (erg/sec)	Ratio
(1)[a]	(2)[b]	(3)[c]	(4)[d]	(5)[e]	(6)[f]	(7)[g]
050730	1	3.97	31.49	6.67E+49	3.26E+49	2.05
050730	2	3.97	31.49	5.61E+49	2.66E+49	2.11
050730	3	3.97	31.49	3.37E+49	2.28E+49	1.48
060124	1	2.30	227.41	1.32E+49	1.34E+51	101.71
060124	2	2.30	227.41	1.12E+49	8.71E+50	77.46
060607A	1	3.082	25.04	1.90E+50	1.34E+49	14.14
060607A	2	3.082	25.04	1.46E+50	9.01E+48	16.21
060714	1	2.71	31.00	1.26E+48	1.10E+50	87.31
060714	2	2.71	31.00	1.17E+48	8.77E+49	75.13
060729	1	0.54	74.87	3.14E+46	1.61E+49	513.17
060814	1	0.84	78.97	3.77E+47	4.55E+49	120.67
080810	1	3.35	24.37	5.50E+48	3.57E+49	6.50

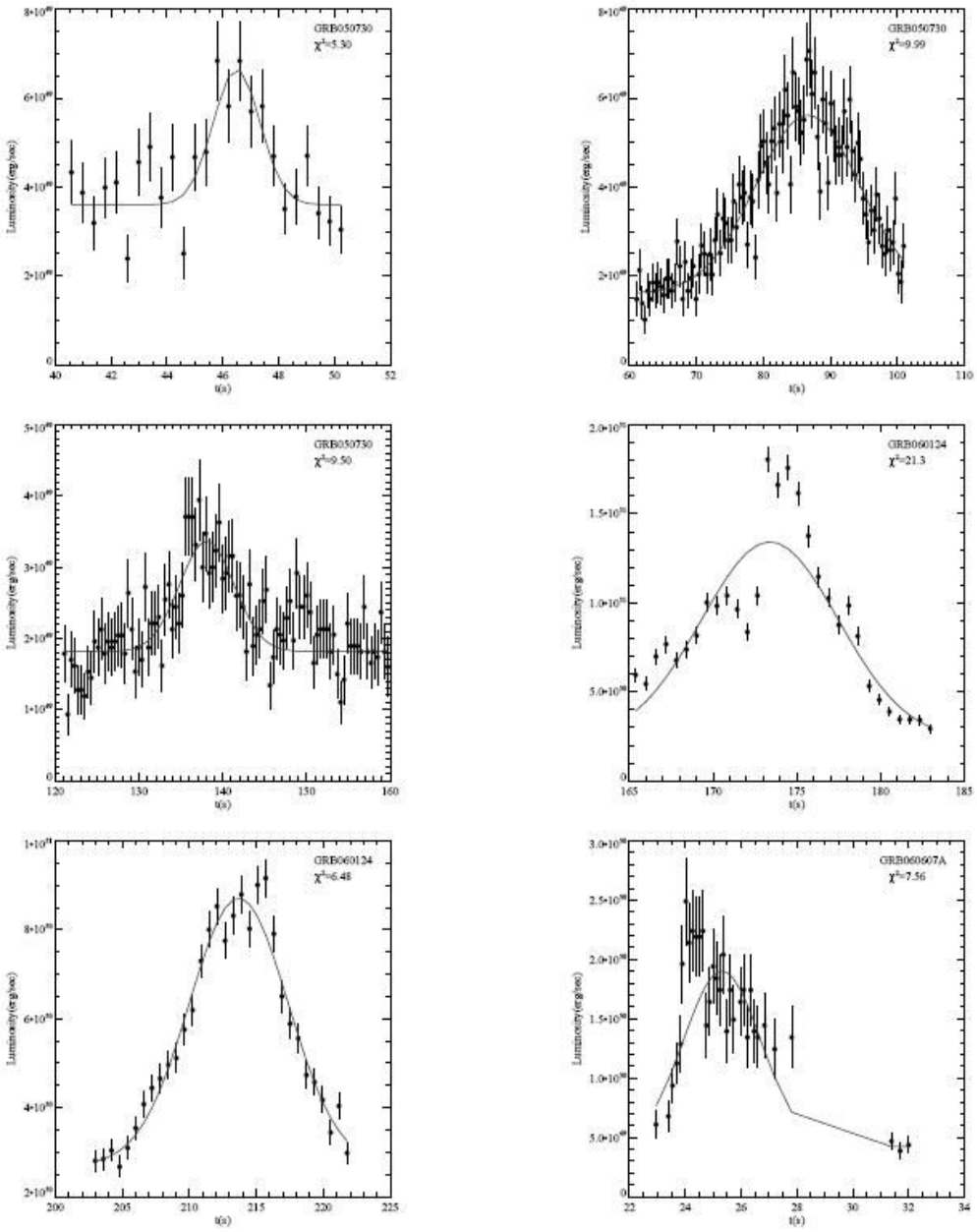

Figure 3.2. Gaussian fit to XRT flares.

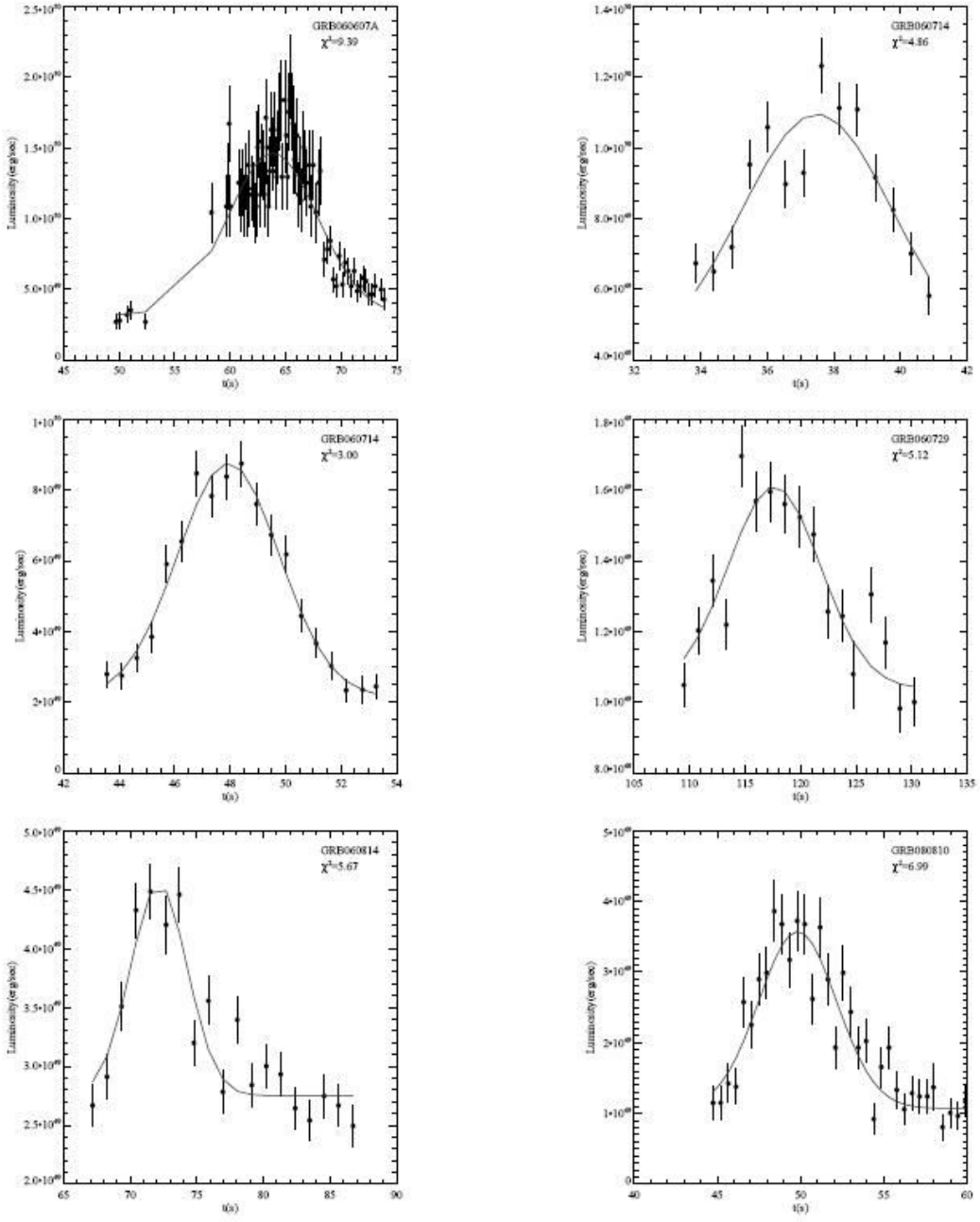

Figure 3.2. Continued.

3.3 Correlations between GRB properties

Correlations among GRB properties are evaluated by Spearman's rank correlation method. Correlation coefficient, ρ, and significance (null hypothesis probability) ,r, are the two parameters that describe this method. In our evaluation, correlation coefficient between 0.55 and 1 with a significance less than 0.001 is satisfactory for a positive correlation. Furthermore, correlation coefficient between -0.55 and -1 with a significance less than 0.001 yields negative correlation. Based on these criteria, the following correlations are concluded:

1- Central engine average γ-ray luminosity, $\bar{L}_{\gamma}$, and total isotropic emission energy in the γ-ray prompt emission, $E_{\gamma,iso}$ have positive correlation (Figure 3.3). $\bar{L}_{\gamma}$ comes from

$$\bar{L}_{\gamma} = \frac{E_{\gamma,iso}}{T_{90,Rest\ Frame}} \tag{4.6}$$

Where

$$T_{90,Rest\ Frame} = \frac{T_{90}}{z} \tag{4.7}$$

Also, no correlation is shown between $E_{\gamma,iso}$ and T_{90}. Therefore, the above correlation shows that more energetic central engine is due to intrinsically higher brightness not longer duration.

2-Total energy emitted during the shallow decay, $E_{plateau}$, and total isotropic emission energy in the γ-ray prompt emission , $E_{\gamma,iso}$ have positive correlation (Figure 3.4). This means that a more energetic central engine yields a more

energetic afterglow. This result is consistent with similar radiative efficiency for all kinds of bursts, short and long (Zhang et al. 2007).

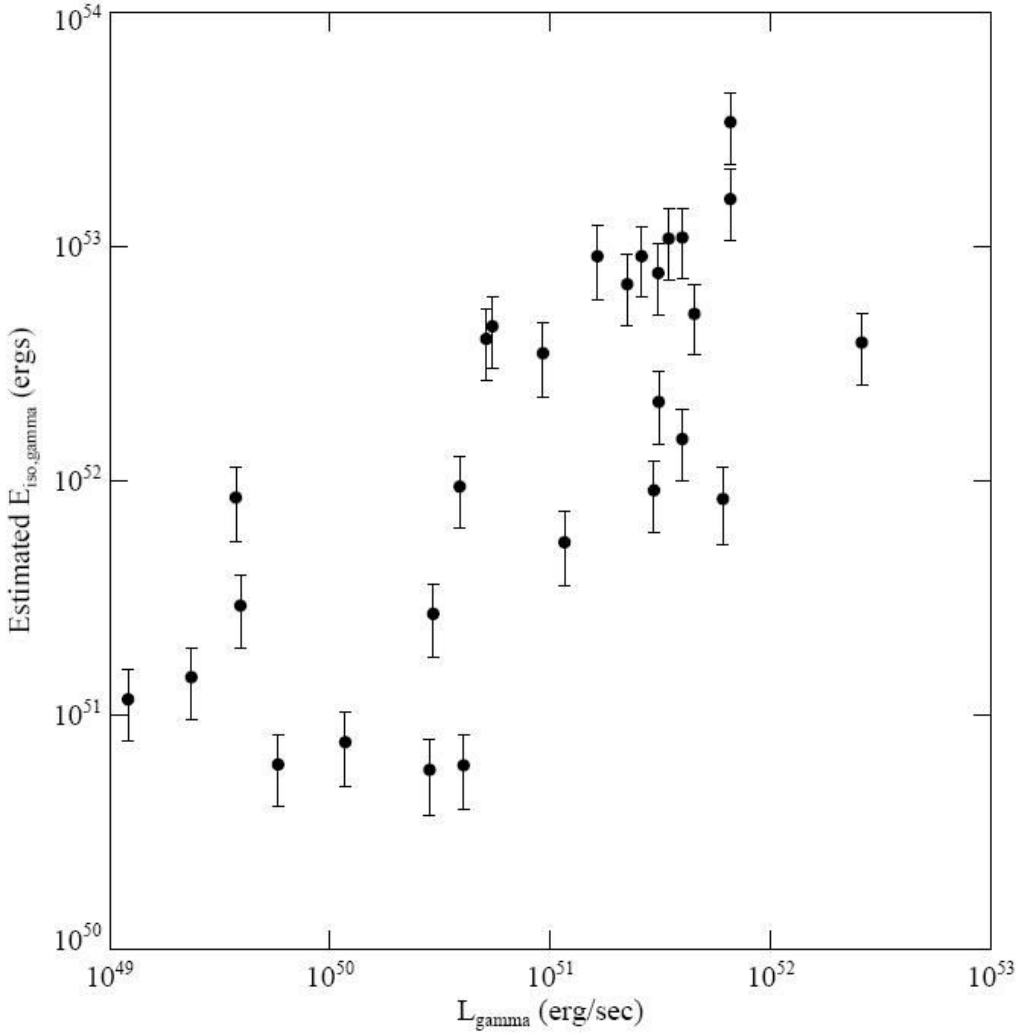

Figure 3.3. Central engine energy against central engine brightness.

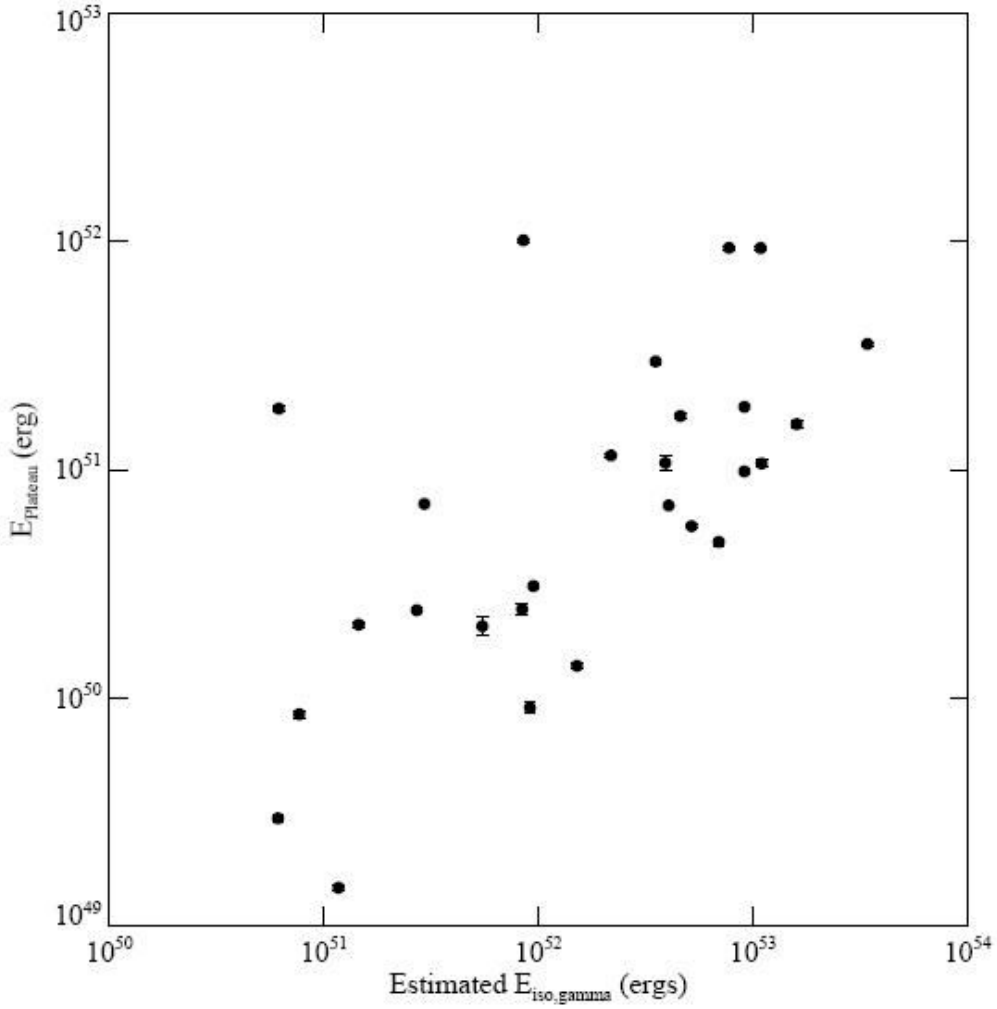

Figure 3.4. Plateau energy against estimated isotropic energy

3-Luminosity at break time and break time have negative correlation (Figure 3.5). Break time could be estimated as shallow decay duration. Therefore, this negative correlation shows that luminosity at break time decreases as shallow decay duration increases.

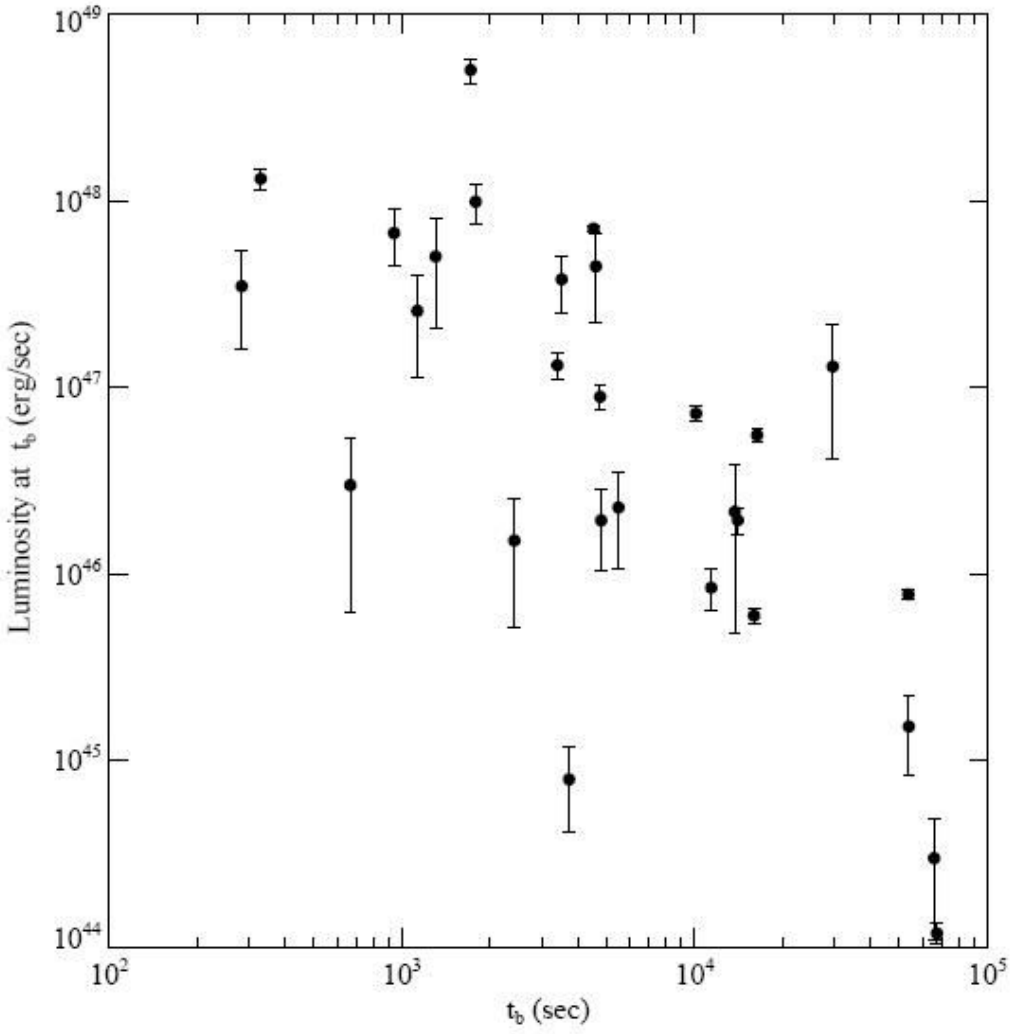

Figure 3.5. Break time luminosity against breaktime

3.4 Evolution of GRB properties

Correlations between GRB properties and redshift are also evaluated by Spearman's rank correlation method. The criteria for correlation are the same as described in the previous section. The following are the existing correlation based on our evaluation:

1-$E_{plateau}$ and redshift are positively correlated (Figure 3.6). This means that GRB afterglow energy increases with redshift.

2-Both $E_{\gamma,iso}$ and $\bar{L}_{\gamma}$ are also positively correlated with redshift. Figure 3.7 and 3.8 show the graph of $E_{\gamma,iso}$ and $\bar{L}_{\gamma}$ versus redshift respectively. However, this increase of $E_{\gamma,iso}$ and $\bar{L}_{\gamma}$ with redshift could be due to instrumental flux threshold (Liang et al. 2007). Maximum redshift for a given luminosity is determined by:

$$F_{th} = \frac{L}{4\pi} z_{max} \tag{3.8}$$

z_{max} is maximum redshift for a given burst with luminosity L and F_{th} is the instrumental flux threshold. So for higher redshift, the detectable luminosity increases given the same flux threshold of the detector.

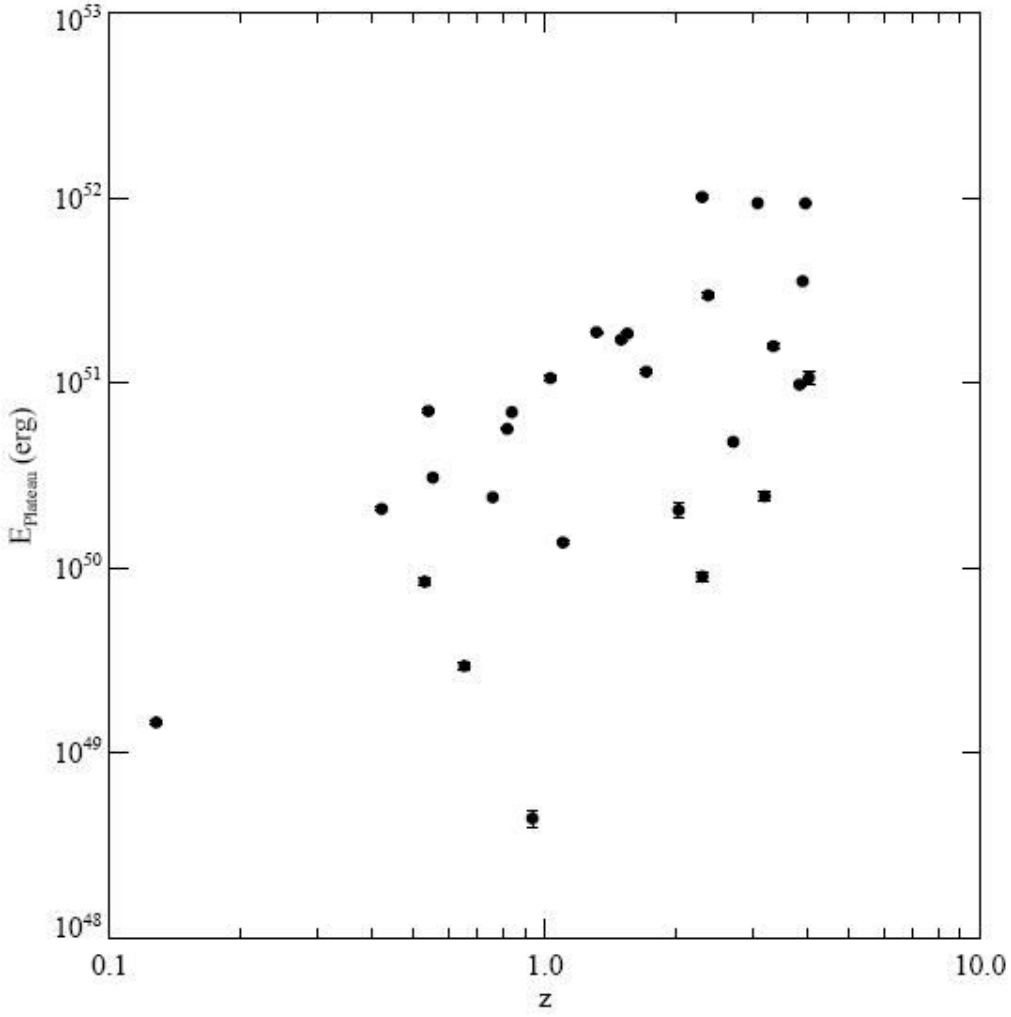

Figure 3.6. Plateau energy against redshift

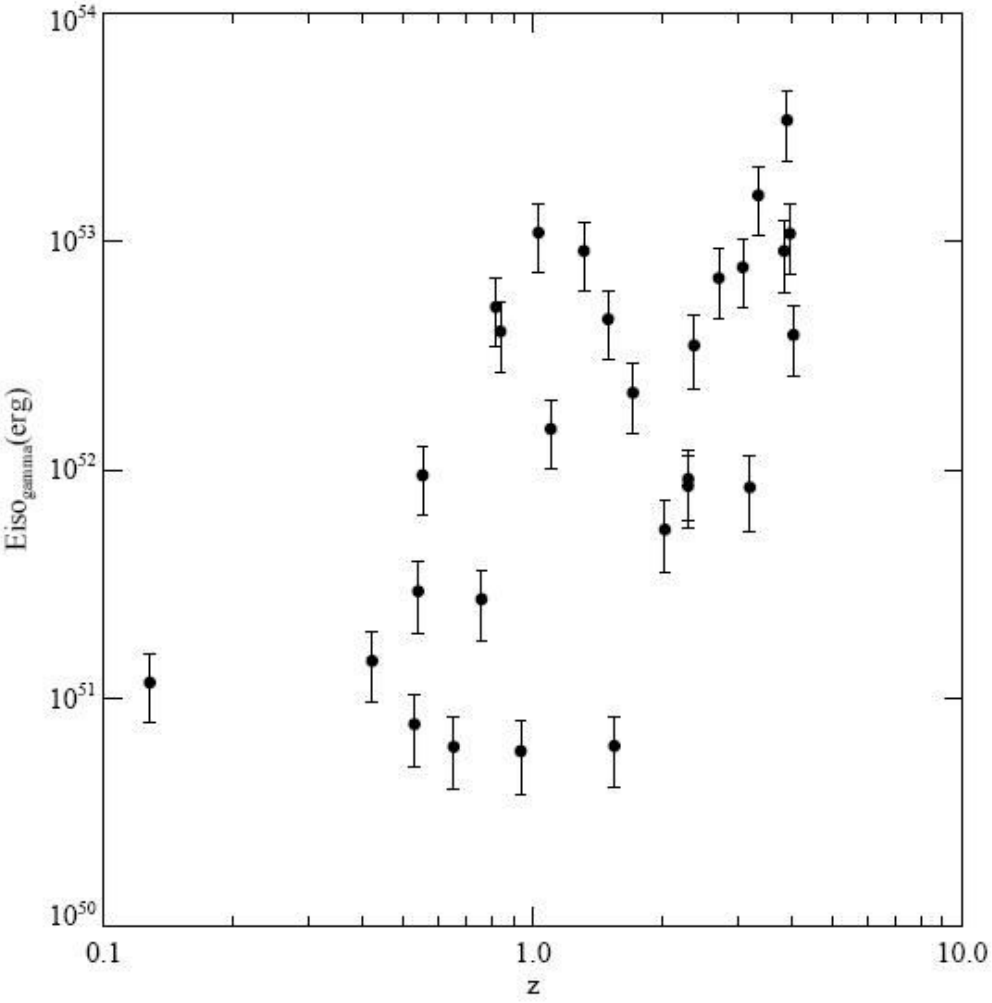

Figure 3.7. Central engine energy against redshift

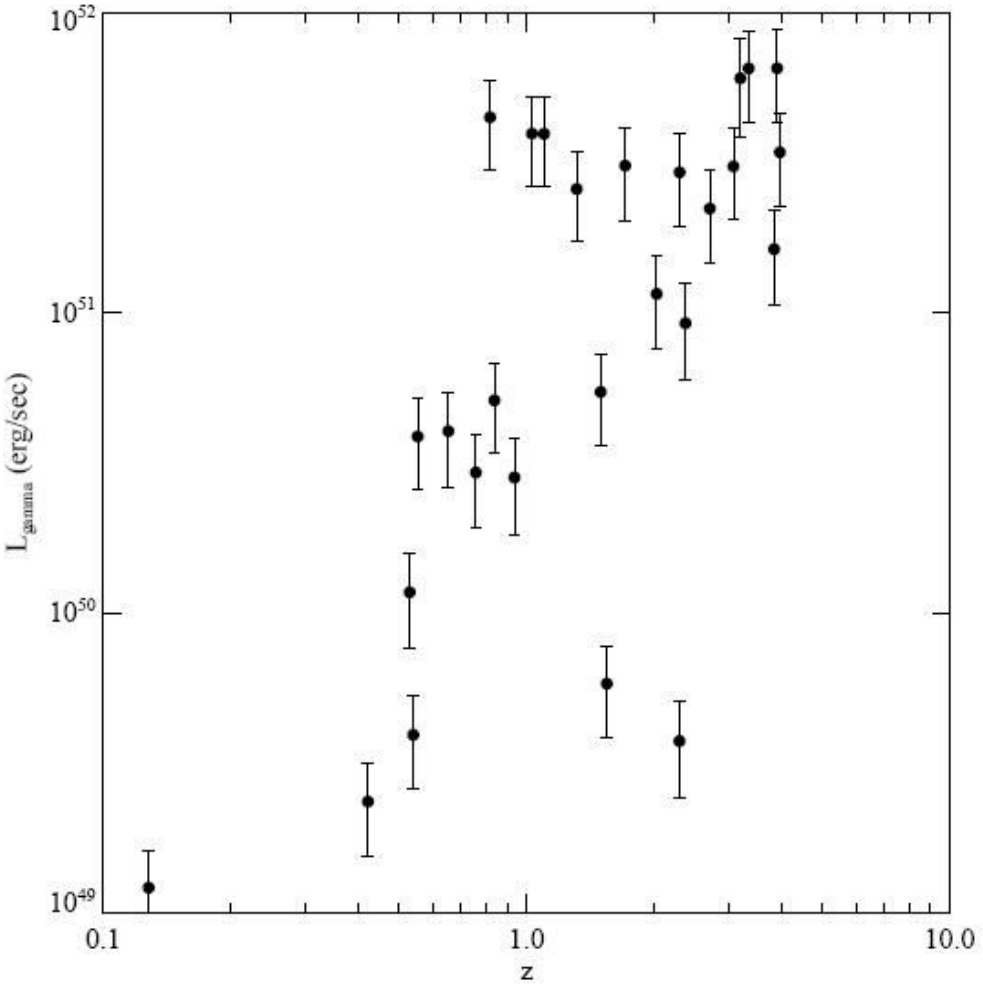

Figure 3.8. Central engine brightness against redshift

3.5 Discussion

In the previous section some GRB property correlations and some GRB property evolution are identified. However, some other correlations and evolutions especially the ones that the defined "Ratio" is involved are hard to assert. For these cases, the correlation coefficient and significance value are close to the values of the suggested criteria and including more GRBs with recognizable flare will validates or disqualifies the relations.

3.6 Conclusion

In this chapter, I examine GRB property correlations and their evolution. some GRB flare-based quantities are also introduced and their correlation with GRB properties and their evolution are studied. The correlation between average luminosity and isotropic γ-ray energy, energy of plateau and isotropic γ-ray energy and luminosity at break time and break time and evolution of plateau energy are well established. It is also realized that the apparent evolution of isotropic γ-ray energy and average luminosity is due to the instrumental flux threshold. Expanding the GRB sample and including more GRBs with XRT flares will provide a chance to reevaluate the discussed correlations and confirm or rule out the hard to assert result due to the limited number of data especially in the cases where x-ray afterglow flare is involved.

Chapter 4

IN SEARCH FOR A RELATION WITH PHYSICAL ORIGIN FOR GRBS

Gamma-ray burst observations provide a great opportunity for cosmography in high redshift. Some tight GRB correlations are already known. The relations with physical origin will have a better potential to utilize GRBs for cosmography. We show here, that analyzing the thermal component of the GRB prompt emission leads us to well-correlated relations. I also perform Monte Carlo tests and show that these correlations are acceptably insensitive to our assumptions. Our correlation looks similar to Ghirlanda's in quality, and provides some physical insights to this relation.

4.1 Introduction

The prompt emission of gamma-ray bursts is commonly modeled as a smoothly broken power law which has been known as the Band function (Band et al. 1993). It was first known that the spectra of Gamma-ray bursts have a non-thermal character over a broad energy range (Fishman & Meegan 1995). This was found to be consistent with the predictions of optically-thin synchrotron emission from a power-law distribution of energetic, relativistic electrons (Katz et al. 1994, Tavani et al. 1996). In spite its success; there are difficulties that the purely non-thermal emission models face (Ghirlanda et al 2003). Introducing an additional optically-thick thermal component that may contribute to the spectrum helps correcting these issues (Meszaros et al. 2002). Ryde et al. (2002) identified a few bursts which are consistent with thermal emission throughout the burst. These bursts

were interpreted as the bursts in which the initial conditions are such that the optically-thick thermal photospheric emission component dominates over the optically-thin emission from the dissipated energy. Therefore, the prompt emission spectrum is interpreted as a composite of a thermal component in addition to the non-thermal one.

Most GRB outflow models assume a single non-thermal dominant component. Thompson et al. (2007) assumes that a second thermal component is essential for undersatnding of the prompt emission of GRBs. They demonstrate that this quasi-thermal model has implications for limitimg the GRB jet Lorenz factor and the mass and radius of the stellar progenitor. The Amati,Ghirlanda, Fermani and Liang & Zhang correlations are also studied within the context of thermalization in relativistic outflow.

In this chapter, I examine the physical properties of GRB thermal component in order to search for a physically motivated correlation among GRB properties. In section 4.2, the physics of blackbody radiation is employed and GRB thermal component flux is calculated. The flux is also estimated for this component. In section 4.3, the analysis of the relations deduced in section 4.2 is presented. I use the Spearman rank correlation analysis to evaluate these relations. I also study the best linear fit for each relation. The derived relations depend on three scaling factors. In section 4.4, the Monte Carlo test is used to examine the sensitivity of my analysis to these scaling factors. I also discuss the implication of these relations. I conclude in section 4.5.

4.2 Thermal emisson component in GRB prompt emission

The Stefan-Boltzmann law states that the power emitted per unit area of the surface of a thermal (blackbody) radiation is directly proportional to the fourth power of its absolute temperature. That is

$$F_{BB} = \sigma T^4 \tag{4.1}$$

where F_{BB} is the power radiated isotropically per unit area by blackbody surface and T is the temperature and $\sigma = 5.67 \times 10^{-8} Wm^{-2}K^{-4}$ is the Stefan-Boltzmann constant. Wien's displacement law states that there is an inverse relationship between the wavelength of the peak of the emission of a black body and its absolute temperature. That is

$$\lambda_{max} = \frac{b}{T} \tag{4.2}$$

where λ_{max} is the peak wavelength, T is the absolute temperature of the blackbody and $b = 2.90 \times 10^{-3} mK$ is Wien's displacement constant. By substituting T from (4.2) into (4.1)

$$F_{BB} = \sigma \left(\frac{b}{\lambda_{max}}\right)^4 \tag{4.3}$$

The peak wavelength, λ_{max}, and the peak energy of the blackbody component, $E_{peak,BB}$, are related through

$$\lambda_{max} = \frac{ch}{E_{peak,BB}} \tag{4.4}$$

Where $c = 3 \times 10^8 ms^{-1}$ is speed of light and $h = 6.63 \times 10^{-34} js$ is Planck's constant. By substituting (4.4) into (4.3)

$$F_{BB} = \sigma \left(b \frac{E_{peak,BB}}{ch} \right)^4 \tag{4.5}$$

The gamma-ray power radiated per unit area by the thermal and non-thermal component of GRB, $\hat{F}_{[E_1,E_2]}$ can approximately be estimated as

$$\hat{F}_{[E_1,E_2]} = \frac{E_{iso,[E_1,E_2]}}{4\pi R^2 T_{90}/(1+z)} \tag{4.6}$$

where T_{90} is the time interval whitin which 90% of the burst fluence is detected and R is the photospheric radius where the thermal radiation occurs. $[E_1, E_2]$ is the co-moving bandpass and $E_{iso,[E_1,E_2]}$ is the estimated isotropic gamma-ray energy radiating from GRB. That is

$$E_{iso,[E_1,E_2]} = \frac{4\pi k D_L^2 S_{[e_1,e_2]}}{(1+z)} \tag{4.7}$$

where D_L is the luminosity distance at the redshift z, k is a k-correction factor to correct the observed gamma-ray fluence at an observed bandpass $[e_1, e_2]$ to a given bandpass in the cosmological rest frame $[E_1, E_2]$.

To eliminate the uncertainty due to the k-correction in $E_{iso,[E_1,E_2]}$ calculation, the more accurate estimation of the flux comes from the fluence in the detector bandpass $[e_1, e_2]$

$$\hat{F}_{[E_1^*,E_2^*]} = \frac{4\pi D_L^2 S_{[e_1,e_2]}/(1+z)}{4\pi R^2 T_{90}/(1+z)} \tag{4.8}$$

where $E_1^* = e_1(1+z)$ and $E_2^* = e_2(1+z)$ and $S_{[e_1,e_2]}$ is the detector bandpass fluence.

$F_{[E_1^*,E_2^*],BB}$ also can be calculated from the integral of the Planck function over co-moving gamma-ray bandpass.

$$F_{BB,[E_1^*,E_2^*]} = \pi \int_{E_1^*}^{E_2^*} B_\nu\,(T) d\nu \tag{4.9}$$

where

$$B_\nu(T) = \frac{2h\nu^3/c^2}{exp(h\nu/KT)-1} \tag{4.10}$$

is the Plank function and $k = 1.38 \times 10^{-23} m^2 kg s^{-2} K^{-1}$ is the Boltzmann constant and υ is the frequency of radiated photon. Substituting (4.4) into (4.2)

$$T = \frac{b}{ch} E_{peak,BB} \tag{4.11}$$

and replacing $h\nu$ by E in (4.10)

$$B_E(T) = \frac{2E^3/c^2h^2}{exp(chE/kbE_{peak,BB})-1} \tag{4.12}$$

and substituting it into (4.9) results in a new form of the Plank function. Therefore,

$$F_{BB,[E_1,E_2]} = \pi \int_{E_1}^{E_2} \frac{2E^3/c^2h^3}{exp(chE/kbE_{peak,BB})-1} dE \tag{4.13}$$

All the above fluxes are calculated or estimated at the photosphere of the burst. In the next section, I introduce some scaling factors. By assuming a representative value for each constant, I look into the correlation between calculated and estimated thermal flux. I later examine the sensitivity of my analysis to these scaling factors.

4.3 Analysis

I peform my analysis for three samples of GRBs: a sample of Swift, a sample of pre-Swift and a sample consisting of the two preceding samples. For the sample of Swift GRBs, I use the Butler et al. (2007) catalog. My sample contains

27 redshift known GRBs with defined upper and lower limits of peak energy from the catalog.

Table 4.1. Swift GRB Sample

GRB	z	T_{90} (s)	$\sigma_{T_{90}}$ (s)	$S_{[15,350]}$ (10^{-6}ergs cm^{-2})	$\sigma_{S_{[15,350]}}$* (10^{-6}ergs cm^{-2})	α	σ_α*	β	σ_{beta}*	E_{peak} (keV)	$\sigma_{E_{peak}}$* (keV)	e1	e2
(1)	(2)	(3)	(4)	(5)	(6)	(7)	(8)	(9)	(10)	(11)	(12)	(13)	(14)
050318	1.44	31	0.1	1.41	0.11	-1.2	0.4	-2.3	0.46	50	10	15	350
050406	2.44	5	1	0.071	0.011	3	2.45	-2.3	0.46	25	21.79	15	350
050525	0.61	9.1	0.07	18.6	0.3	-0.8	0.1	-2.3	0.46	81	3	15	350
050814	5.3	28	3	0.8	0.1	0	1	-2.3	0.46	64	36.33	15	350
050922c	2.198	4.6	0.2	2.7	0.24	-1	0.3	-2.3	0.46	183	121.18	15	350
051109a	2.346	4.9	0.5	1.56	0.11	1	1.73	-2.01	0.079	110	106.92	15	350
051109B	0.08	8.3	0.7	0.17	0.024	0	1.41	-2.3	0.46	50	14.14	15	350
051111	1.55	17	1	7	0.75	-1	0.3	-2.3	0.46	233	184.97	15	350
060115	3.53	110	1	1.9	0.24	-1.1	0.6	-2.3	0.46	68	25.40	15	350
060124	2.296	8.2	0.3	0.48	0.03	5	2	-2.01	0.20	83	92.09	15	350
060206	4.045	6.1	0.3	1.04	0.089	-1.2	0.3	-2.3	0.46	83	23.66	15	350
060218	0.0331	128	4	0.79	0.12	-0.8	1.095	-2.3	0.46	41	22.58	15	350
060223a	4.41	8.4	0.4	0.68	0.0878	-1	0.6	-2.3	0.46	75	29.88	15	350
060428b	0.348	20	1	0.36	0.05	5	5	-3.1	0.55	20	10.95	15	350
060510b	4.9	230	4	4.4	0.49	-1.4	0.4	-2.3	0.46	76	34.64	15	350
060522	5.11	74	4	1.2	0.28	-0.7	0.89	-2.3	0.46	90	78.96	15	350
060605	3.78	19	1	0.61	0.12	-0.3	0.79	-2.3	0.46	142	133.98	15	350
060607a	3.082	103	4	3.7	0.45	-1	0.3	-2.3	0.46	139	94.54	15	350
060707	3.425	75	3	1.9	0.37	-0.7	0.8	-2.3	0.46	64	18.71	15	350
060708	1.8	7.5	0.8	0.65	0.084	-1	0.5	-2.3	0.46	99	59.48	15	350
060904B	0.703	75.2	0.9	1.9	0.39	-1	0.7	-2.3	0.46	83	56.57	15	350
060908	2.43	18.5	0.3	4.1	0.4	-0.8	0.3	-2.3	0.46	161	82.14	15	350
060927	5.6	23	0.4	1.32	0.19	-0.8	0.4	-2.3	0.46	73	16.61	15	350
070208	1.165	52	1	0.57	0.11	0	1.41	-2.3	0.46	66	76.86	15	350
070419a	0.97	160	14	0.54	0.085	0	2	-2.3	0.46	27	17.43	15	350
070506	2.31	3.6	0.3	0.2	0.01	5	3	-2.01	0.06	71	48.73	15	350
070508	0.82	21.2	0.4	33	1	-1	0.1	-2.3	0.46	208	55.82	15	350

* when asymetric errors are reported, $\sigma = \sqrt{\sigma^+\sigma^-}$ is assumed.

The data is shown in table 4.1 with the following heading: (1) GRB name; (2) redshift; (3) BAT T_{90}; (4) BAT T_{90} error; (5) γ-ray fluence; (6) γ-ray fluence error; (7) low-energy spectral index; (8) low-energy spectral index error; (9) high-energy spectral index; (10) high-energy spectral index error; (11) spectral peak energy; (12) spectral peak energy error; (13) lower limit of BAT detector band-pass; (14) higher limit of BAT detector band-pass.

Table 4.2. Pre-Swift Data Sample

GRB	z	T_{90} (s)	$S_{[e1,e2]}$ (10^{-6}ergs cm^{-2})	$\sigma_{S_{[e1,e2]}}$ (10^{-6}ergs cm^{-2})	α	σ_α	β	σ_{beta}	E_{peak} (keV)	$\sigma_{E_{peak}}$ (keV)	e1	e2
970228	0.695	80	11	1	-1.54	0.08	-2.5	0.4	115	38	40	700
970828	0.957	146.59	96	9	-0.70	0.08	-2.07	0.37	298	59	20	2000
971214	3.42	35	8.8	0.9	-0.76	0.1	-2.7	1.1	155	30	40	700
980425	0.0085	37.41	3.8	0.4	-1.266	0.13	-2.3	0.46	118	24	20	2000
980613	1.096	20	1	0.2	-1.43	0.24	-2.7	0.6	93	43	40	700
980703	0.966	102.37	23	2	-1.31	0.14	-2.39	0.26	255	51	20	2000
990123	1.6	100	300	40	-0.89	0.08	-2.45	0.97	781	62	40	700
990506	1.3066	220.38	190	20	-1.37	0.15	-2.15	0.38	283	57	20	2000
990510	1.619	75	19	2	-1.23	0.05	-2.7	0.4	163	16	40	700
990705	0.843	42	75	8	-1.05	0.21	-2.2	0.1	189	15	40	700
990712	0.43	20	6.5	0.3	-1.88	0.07	-2.48	0.56	65	11	40	700
991216	1.02	24.9	190	20	-1.234	0.13	-2.18	0.39	318	64	20	2000
000131	4.5	110.1	42	4	-0.688	0.08	-2.07	0.37	130	26	20	2000
000214	0.42	10	14	0.4	-1.62	0.13	-2.1	0.0	82	5	40	700
000911	1.058	500	220	20	-1.11	0.12	-2.32	0.41	579	116	15	8000
010222	1.473	130	93	3	-1.35	0.19	-1.64	0.02	358	10	40	700
010921	0.45	24.6	10	1	-1.49	0.16	-2.3	0.0	106	21	30	700
020124	3.2	78.6	6.8	0.7	-1.0	0.11	-2.3	0.41	110	22	30	400
020405	0.69	60	74	7	-0.0	0.25	-1.87	0.23	364	73	15	2000
020813	1.25	90	100	10	-1.05	0.11	-2.3	0.0	211	42	30	400
021211	1.01	2.41	2.2	0.2	-0.85	0.09	-2.37	0.42	47	9	30	400
030226	1.98	76.8	6.4	0.6	-0.95	0.1	-2.3	0.0	108	22	30	400
030328	1.52	140	26	2	-1.0	0.11	-2.3	0.0	110	22	30	400
030329	0.1685	23	110	10	-1.26	0.02	-2.28	0.05	68	2	30	400

For pre-Swift GRBs, Ghirlanda et al. (2004) data is used. In my sample, I eliminate the GRBs whose spectral indices, peak energy, duration or fluence is missing. The data is shown in table 4.2. This sample consists of 24 pre-Swift GRBs. It should be noted that all GRBs in my samples are considered long.

Not all physical quantities involved in the calculated and estimated fluxes derived in section 4.2 are known. To use these equations, we consider the following assumptions:

First, Ryde et al. (2009) finds that for their sample of 56 long BATSE GRBs the ratio of the thermal (blackbody) flux over the total flux is approximately 30%-50%. The thermal flux is the bolometric integrated blackbody flux and the total flux is integrated over the energy band ~25-1900 kev. Therefore, the ratio found is the upper limit to the true unknown bolometric ratio. Ryde et al. (2009) also notes that this ratio varies in time and no strong trend is observed. Here, I assume 40% for the ratio

$$F_{BB,[E_1,E_2]} \cong AF_{[E_1,E_2]} \tag{4.16}$$

where $A = 0.4$.

Second, the photospheric radius is the radius above which the flow becomes optically thin to scattering by the baryon related electrons. All of the GRBs in our sample are considered long. Long GRBs are associated with the death of massive stars. Typical the radius of a massive star is 10-100$R_{\odot}$. Also, Pe'er et al. (2010b) shows that the photospheric radius of GRB090902B, which is also considered to

be a long GRB, is roughly $6.1 - 7.8 \times 10^9 m$. Here, I take a representative photospheric radius to be $10R_\odot$

$$R \cong CR_\odot \tag{4.15}$$

where $R_\odot = 6.955 \times 10^8 m$ and $C = 10$. Later in section 4.4, the estimation of photospheric radius is discussed in more details.

Third, Ryde et al. (2009) also shows that the peak energy of GRB spectra, E_{peak}, is defined by the thermal component peak energy, $E_{peak,BB}$. However, they do not necessarily coincide. Combination the of thermal component with the positively-sloped power law non-thermal component shifts the peak energy of GRB thermal component to a higher energy. Therefore, I make the assumption that $E_{peak,BB}$ is a large fraction of E_{peak} in the range of ~80%-100%. Here I take 90% for this fraction.

$$E_{peak,BB} \cong DE_{peak} \tag{4.16}$$

where $D = 0.90$.

Some of the above assumptions may seem to be the result of oversimplification. However, I carefully consider the possible range for each scaling factor. Then in the next section, I apply a Monte Carlo test and evaluate my correlation results.

Some remarks about my notation might be helpful. All F's are the flux from either Planck's law integration or the Stefen-Boltzman law which is the result of integration of Planck' law over the full range of spectrum and all the $\hat{F}$'s are from the flux estimation. Any quantity for the thermal component is shown by a BB

index. If no index is shown, it means that quantity belongs to combination of thermal and non-thermal component. Also if a specific range of energy does not come in the index of a quantity, that quantity is bolometric. In this work, I evaluate the following relations:

1- Applying the third assumption, (4.5) results in the bolometric integrated blackbody flux

$$F_{BB} = \sigma \left(b \frac{DE_{peak}(1+z)}{ch} \right)^4 \tag{4.17}$$

$DE_{peak}(1+z)$ replaces the comoving peak energy for the thermal component. E_{peak} is peak energy of GRB spectra. From equation (4.6) and applying the first and second assumption, the estimated flux for co-moving bandpass $1 - 10^4$ kev is

$$\hat{F}_{BB,[1kev,10^4kev]} = A \frac{E_{iso,[1kev,10^4kev]}}{4\pi C^2 R^2 T_{90}/(1+z)} \tag{4.18}$$

and

$$\hat{F}_{BB} = AB \frac{E_{iso,[1kev,10^4kev]}}{4\pi C^2 R^2 T_{90}/(1+z)} \tag{4.19}$$

where $\hat{F}_{BB}$ is the estimated thermal flux and B is the ratio of bolometric thermal flux over isotropic gamma-ray flux for co-moving bandpass $1 - 10^4$ kev

$$B = \frac{F_{BB}}{F_{BB,[1kev,10^4kev]}} \tag{4.20}$$

where

$$F_{BB,[1kev,10^4kev]} = \pi \int_{1kev}^{10^4kev} \frac{2E^3/c^2h^3}{exp(chE/kbDE_{peak}(1+z))-1} dE \tag{4.21}$$

B equals to one to 5 degrees of magnitude. Therefore, co-moving bandpass 1-10^4 kev is considered as bolometric bandpass for GRBs.

$$\hat{F}_{BB} = A\frac{E_{iso,[1kev,10^4kev]}}{4\pi C^2R^2T_{90}/(1+z)} \tag{4.22}$$

By comparing (4.17) and (4.21), it is apparent that gamma-ray isotropic enery is directly proportional to the fourth power of comoving peak energy if the correlation between F_{BB} and $\hat{F}_{BB}$ exists.

2- Use of K-correction in calculation of $E_{iso,[E_1,E_2]}$ causes uncertainty in the flux calculation. Bloom et al. (2001) shows, the typical estimated uncertainty on a given k-corrected energy is ~20%. To eliminate this source of uncertainty, I use the flux in the co-moving bandpass $[e_1(1+z), e_2(1+z)]$. $[e_1, e_2]$ is the detector bandpass . Therefore, from equation (4.7) and applying the first and third assumption

$$\hat{F}_{BB,[e_1(1+z),e_2(1+z)]} = A\frac{4\pi D_L^2 S_{[e_1,e_2]}/(1+z)}{4\pi C^2R^2T_{90}/(1+z)} \tag{4.23}$$

also from equation (4.13) and applying the third assumption, the integral of the Planck function over the co-moving bandpass $[e_1(1+z), e_2(1+z)]$ is

$$F_{BB,[e_1(1+z),e_2(1+z)]} = \pi\int_{e_1(1+z)}^{e_2(1+z)}\frac{2E^3/c^2h^3}{exp(chE/kbDE_{peak}(1+z))-1}\,dE \tag{4.24}$$

In the case of the correlation between $F_{BB,[e_1(1+z),e_2(1+z)]}$ and $\hat{F}_{BB,[e_1(1+z),e_2(1+z)]}$, the proportionality between gamma-ray isotropic energy and the fourth power of comoving peak energy seen before is investigated here. By changing the variable in the integral in equation (4.24)

$$F_{BB,[e_1(1+z),e_2(1+z)]} = \frac{2\pi}{c^2h^3}\left(\frac{kbDE_{peak}(1+z)}{ch}\right)^4 \int_{u_1}^{u_2} \frac{u}{exp(u)-1}\,du \tag{4.25}$$

where

$$u = \frac{chE}{kbDE_{peak(1+z)}} \tag{4.26}$$

$$u_1 = \frac{che_1}{kbDE_{peak}} \tag{4.27}$$

and

$$u_2 = \frac{che_2}{kbDE_{peak}} \tag{4.28}$$

By comparing (4.18) and (4.24) and also (4.22) and (4.24), it can be seen that E_{iso} and S are directly proportional to E_{peak}^4 respectively, if the flux correlation exists. However, the integral limits of $\int_{u1}^{u2} \frac{u}{\exp(u)-1}\,du$ depend on E_{peak}. Therefore, to claim these proportionalities the dependency of this unitless integral on E_{peak} should be examined.

Using Spearman rank correlation analysis, I evaluate the discussed correlations for the tree samples in the next section. In this analysis, the same value is considered for each scaling constant for all GRBs. Then, each scaling constant for each GRB is randomly picked from its possible range in the Monte Carlo test and the correlation is examined by the Spearman rank correlation analysis. In section 4.4, We also study the best linear fit and the scatter of data for the two correlations.

4.4 Discussion

Ghirlanda's relation $\left(E_{peak} - E_{\gamma}\right)$ is one of the less wide scattered GRB correlations which is widely accepted and used as standard candle (Ghirlanda et al. 2004; Friedman et al. 2005; Ghirlanda et al. 2009). This correlation is between rest frame peak energy and collimation corrected energy of GRB. GRBs are thought to be collimated sources. In other words, the energy per unit of steradian in the jet is assumed to be uniform inside half-angle, θ_{jet} and zero outside (Rhoads 1997). Therefore, under the standard GRB model assumptions the jetted outflow should produce a break in the afterglow light curve decay. This break time , t_{jet}, allows to deduce the jet openning angle, θ_{jet}.

$$E_{\gamma} = E_{iso}\left(1 - cos\theta_{jet}\right) \tag{4.29}$$

The geometry-corrected E_{γ} reduces the large dispersion of $E_{peak} - E_{iso,\gamma}$ relation (Ghirlanda et al. 2009).

As discussed in the last section, we examin $F_{BB} - \hat{F}_{BB}$ and $F_{BB,[e_1(1+z),e_2(1+z)]} - \hat{F}_{BB,[e_1(1+z),e_2(1+z)]}$ relations. For convenience , we refer to these two relations as "bolometric" and "detector band-pass" respectively. The result of Spearman rank correlation analysis for these two relations for each set of data is presented in table 4.3, 4.4 and 4.5. Correlation coefficient of greater than 0.55 accompanied by correlation siginificance of less than 0.001 is considered criteria for a positive correlation. The result for all three samples shows that a positive correlation certainly exists in both cases. However, All three samples show "detector band-pass" is better correlated. This could be due to the

elimination of K-correction and more accurate use of T_{90} in the estimation of "detector band-pass" flux. As it is mentioned in the last section, using k-correction for estimating "bolometric" flux introduces some uncertainity. Also, T_{90} is the time interval within which 90% of the burst fluence is detected. So, it is most accurate to use it for the estimation in the fluence detector band-pass.

Table4.3. Spearman Rank Correlation Analysis for Swift Data

Calculateded	Estimated	Correlation Coefficient	Correlation Significance
$logF_{BB}$	$log\hat{F}$	0.81	4.07×10^{-7}
$logF_{BB,[15(1+z)kev,350(1+z)kev]}$	$log\hat{F}_{BB,[15(1+z)kev,350(1+z)kev]}$	0.81	3.05×10^{-7}

Table4.4. Spearman Rank Correlation Analysis for pre-Swift Data

Calculateded	Estimated	Correlation Coefficient	Correlation Significance
$logF_{BB}$	$log\hat{F}$	0.70	1.56×10^{-4}
$logF_{BB,[e1(1+z),e2(1+z)]}$	$log\hat{F}_{BB,[e1(1+z),e2(1+z)]}$	0.74	4.06×10^{-5}

Table4.5. Spearman Rank Correlation Analysis for All Data

Calculateded	Estimated	Correlation Coefficient	Correlation Significance
$logF_{BB}$	$log\hat{F}$	0.73	1.03×10^{-9}
$logF_{BB,[e1(1+z),e2(1+z)]}$	$log\hat{F}_{BB,[e1(1+z),e2(1+z)]}$	0.77	5.89×10^{-11}

Friedman et al. (2005) evaluates the geometery-corrected Ghirlanda's relation in the co-moving bandpass $[1 - 10^4]$ kev for their sample of 19 Swift and pre-Swift GRBs by Spearman rank correlation analysis. Their result is 0.83 for the correlation coefficient and 1.2×10^{-5} for the correlation significance. This result is comparable with my result for Swift sample. Correlation coefficient is 0.81 for both correlations and 4.7×10^{-7} and 3.05×10^{-7} for "bolometric" and "detector band-pass" respectively. The Spearman rank correlation analysis result for the other two samples is still considerable. Correlation coefficient ranging between 0.70 to 0.77 and correlation significance better than 1.56×10^{-4} is significant. However, Friedman et al. (2005) considers the Geometry-corrected energy in their analysis. Collimation-corrected energy might improve my result the same way it does for $E_{peak} - E_{\gamma}$ in respect to $E_{peak} - E_{iso}$.

I also study the best linear fit for each relation and look at the scatter of data. The result is shown in table 4.6, 4.7 and 4.8.

Table4.6. Best Linear Fit for Swift Data

Calculateded	Estimated	a	σa	b	Reduced χ^2
$logF_{BB}$	$log\hat{F}$	0.82	0.098	0.47	0.66
$logF_{BB,[15(1+z)kev,350(1+z)kev]}$	$log\hat{F}_{BB,[15(1+z)kev,350(1+z)kev]}$	0.77	0.097	1.77	0.71

Table4.7. Best Linear Fit for Pre-Swift Data

Calculateded	Estimated	a	σa	b	Reduced χ^2
$logF_{BB}$	$log\hat{F}$	0.49	0.15	9.57	1.24
$logF_{BB,[e1(1+z),e2(1+z)]}$	$log\hat{F}_{BB,[e1(1+z),e2(1+z)]}$	0.50	0.14	9.20	1.20

Table4.8. Best Linear Fit for All Data

Calculateded	Estimated	a	σa	b	Reduced χ^2
$logF_{BB}$	$log\hat{F}$	0.66	0.09	4.75	0.94
$logF_{BB,[e1(1+z),e2(1+z)]}$	$log\hat{F}_{BB,[e1(1+z),e2(1+z)]}$	0.64	0.08	5.22	0.93

Here, the calculated value of flux is considered as independent variable while the estimated value is considered as independent variable. In the tables the slope of

the linear fit, a, and its uncertainity, y-intercept and the reduced χ^2 is presented. If there was no assumption for the values of the three scaling constants, A, B and C, and their value was accurate, the slope and y-intercept are expected to be one and zero respectively. However, to study the existence of the discussed correlations and for simplification I consider the same fixed values of scaling constants for all GRBs. Although the slope and y-intercept values are not exactly as they were expected especially in the fit for the pre-Swift sample, the reduced χ^2 (χ^2/the number of GRBs in sample -3)) ranging from 0.66 to 1.24 is satisfactory. Friedman et al. (2005) result of the reduced χ^2 for geometry-corrected Ghirlanda's relation in the co-moving bandpass $[1, 10^4]$ kev for their sample of 19 Swift and pre-Swift GRBs is 4.15. Ghirlanda et al. (2009) shows the reduced χ^2 value of 1.4 for their sample of 29 GRBs. Figure 4.1 shows the best linear fit for the best correlated relation which is the "bolometric" correlation in the analysis for Swift sample (solid line). The criteria for the best correlation is the best Spearman rank correlation test result and the one whoes slope and y-intercept for its linear fit is closest to one and zero and its reduced χ^2 is the least. For the Swift sample, the "bolometric" correlation results in correlation coefficient of 0.81, correlation significance of 4.07×10^{-7}, slope of 0.82, y-intercept of 0.47 and reduced χ^2 of 0.66. The dashed line in this graph shows the ideal case when the slope is one and there is no y-intercept. If the real value of each scaling constant for each GRB is used, the fit will be close to the dashed line.

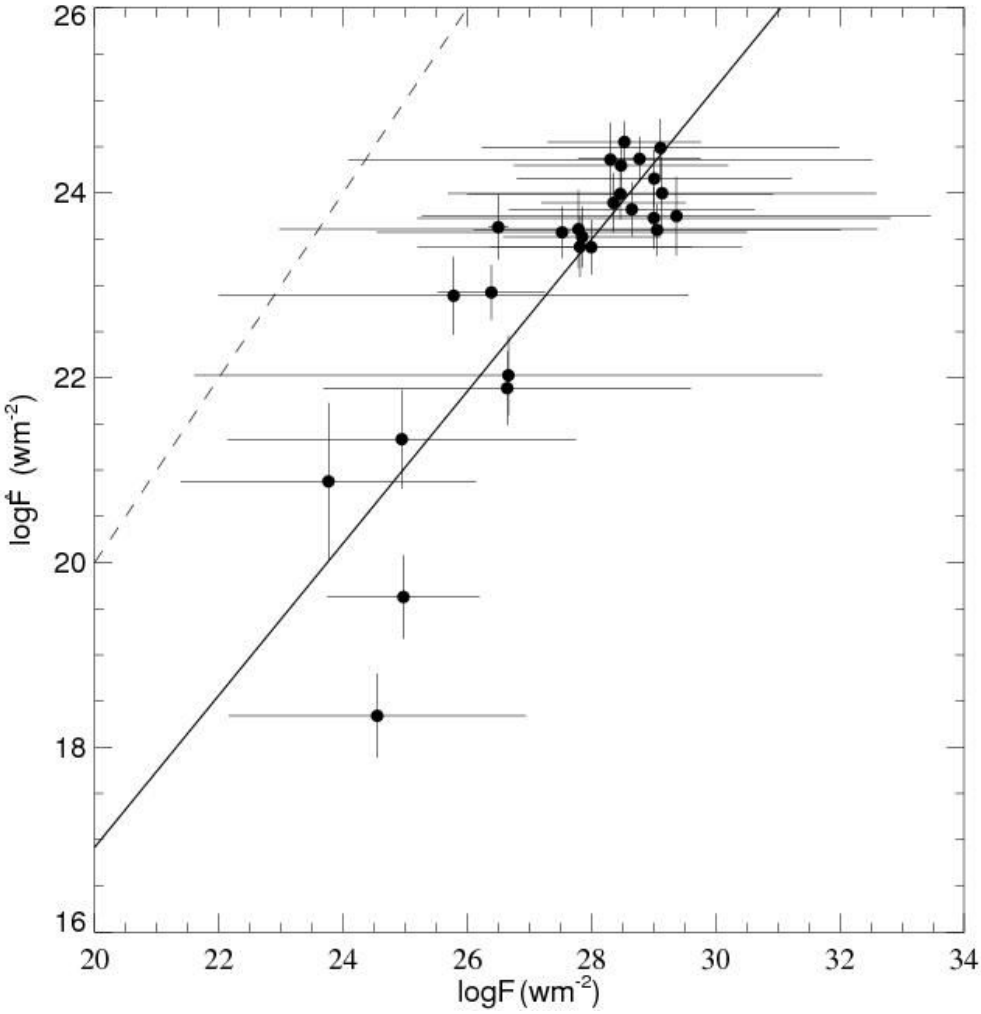

Figure4.1. Graph of estimated bolometric flux versus calculated bolometric flux for Swift data. *Solid line* shows the best linear fit for the data. *Dashed line* shows the ideal case when the slope is one and there is no y-intercept.

A Monte Carlo test is performed to evaluate the discussed correlations. Every scaling constant for each GRB is randomly picked from its possible range. These

ranges consist of: $0.30 \leq A \leq 0.50$, $1 \leq C \leq 100$ and $0.80 \leq D \leq 1$. Table 4.9, 4.10 and 4.11, shows the test result for each sample.

Table 4.9. Monte Carlo Test Result for Swift Data

Calculateded	Estimated	Number of experiments	Number of successes*
$logF_{BB}$	$log\hat{F}$	1000	836
$logF_{BB,[15(1+z)kev,350(1+z)kev]}$	$log\hat{F}_{BB,[15(1+z)kev,350(1+z)kev]}$	1000	848

* The success for the test is defined as correlation coefficient being greater than o.55 and correlation significance is less than 0.001 simultaneously.

Table 4.10. Monte Carlo Test Result for Pre-Swift Data

Calculateded	Estimated	Number of experiments	Number of successes
$logF_{BB}$	$log\hat{F}$	1000	245[a]
$logF_{BB,[15(1+z)kev,350(1+z)kev]}$	$log\hat{F}_{BB,[15(1+z)kev,350(1+z)kev]}$	1000	376[b]

[a] This is the number of experiments that fulfill both success conditions. 440 experiments satisfy only correlation coefficient criteria.
[b] This is the number of experiments that fulfill both success conditions. 594 experiments satisfy only correlation coefficient criteria.

Table 4.11. Monte Carlo Test Result for All Data

Calculateded	Estimated	Number of experiments	Number of successes
$logF_{BB}$	$log\hat{F}$	1000	732
$logF_{BB,[15(1+z)kev,350(1+z)kev]}$	$log\hat{F}_{BB,[15(1+z)kev,350(1+z)kev]}$	1000	818

The success for the test is defined as correlation coefficeint being greater than o.55 and correlation significance being less than 0.001 simultaneously. The number of success of the test for 1000 experiments shows that the correlations are acceptably insensitive to the values of scaling constants for Swift and combined sample. The experiments with success for these data sets include %73-%84.8 of the experiments. However, the result for the pre-Swift data is not satisfactory. Figure 4.2 shows the histogram for the outcome of the Monte Carlo test. The vertical dashed line shows the correlation coefficeint of 0.55.

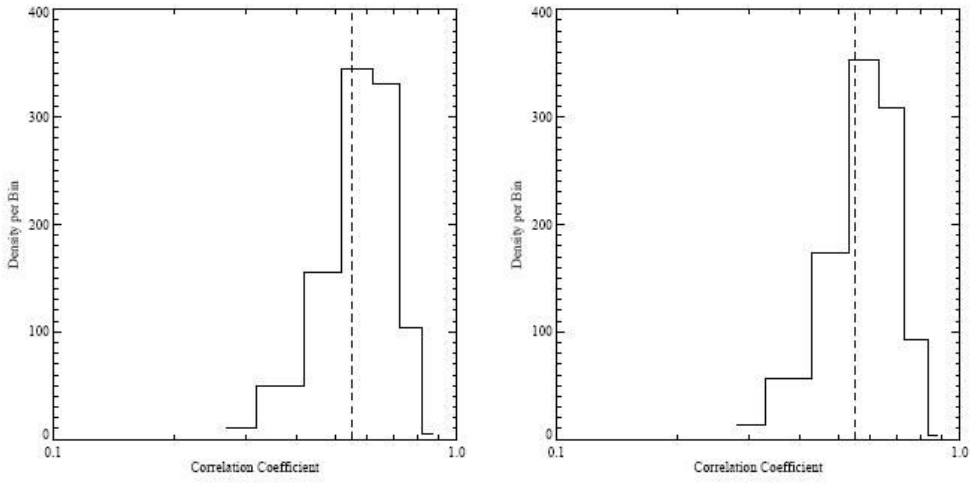

Figure4.2. Histogram of correlation coefficient for Monte Carlo test. *Left graph* shows the result for "bolometric" correlation and *right graph* belongs to "detector band-pass" correlation. The vertical dashed line shows the correlation coefficient of 0.55. In both graphs, for all the experiments on the right side of the dashed line.

In a fixed range of co-moving energy as the integrated thermal flux increases with increase of temprature of blackbody, the energy where the thermal spectrum peaks, E_{peak}, increases. This also can be seen in (4.17). Comparing (4.17) and (4.18) implies Ghirlanda's relation $E_{peak} - E_{\gamma}$. "Bolometric correlation" shows that the gamma-ray energy for bolometric co-moving bandpass $1 - 10^4$ kev is proportional to the fourth power of peak energy. The existence of such a relation is also examined in "detector band-pass" correlation. Comparing (4.18) and (4.24) and also (4.22) and (4.24), it can be seen that E_{iso} and S are directly proportional to E_{peak}^4 respectively. However, the integral limits of $\int_{u1}^{u2} \frac{u}{\exp(u)-1} du$ are expressed in terms of E_{peak} as it is shown in (4.27) and (4.28). Therefore, the dependency of this unitless integral on E_{peak} should be examined. Figure 4.3 shows the graph of this integral verus E_{peak} for Swift and Pre-Swift sample. This integral, I, is calculated for both "bolometric" and "detector band-pass" correlations. Figure 4.3 shows that the integral for bolometric band-pass is a constant for both Swift and pre-Swift samples. In the case of detector band-pass, it is also shown that the value of the integral, I, for Swift peak energy greater than 50 kev and pre-Swift peak energy greater than 100 kev, is roughly a constant. For the Swift sample, the mean of the integral for peak energy greater than 50 kev is 6.20 with a standard deviation of 0.20. For pre-Swift sample, the mean of the integral for peak energy greater than 100 kev is 6.11 with a standard deviation of 0.44.

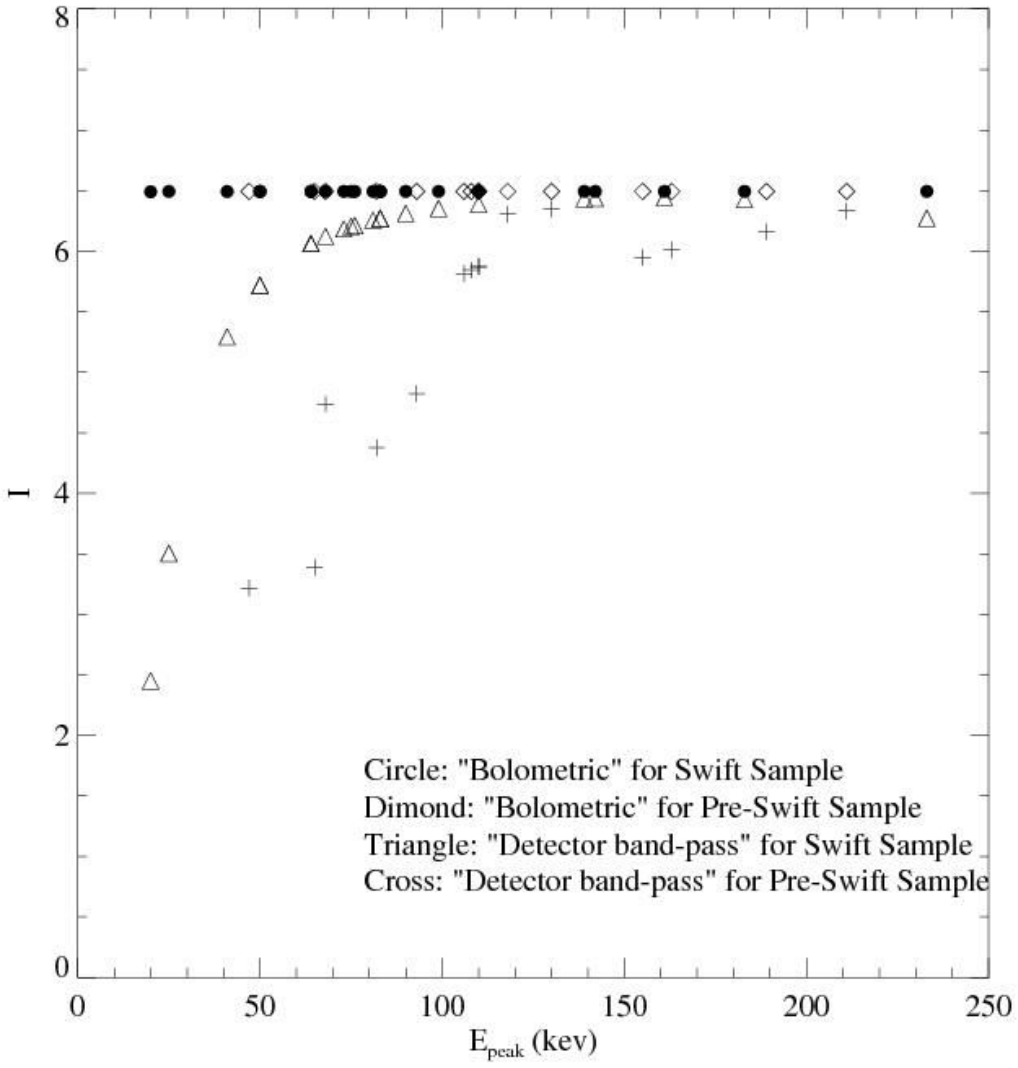

Figure4.3. $I(E_{peak})$ versus E_{peak} for Swift and pre-Swift data. *Filled circles* show the result for Swift data and *unfilled squares* show the result for pre-Swift data. $\int_{u1}^{u2} \frac{u}{\exp(u)-1} du$ is a part of calculated "detector band-pass" as it is shown in section (2.3).

Although the $E_{peak}^4 - E_{\gamma,iso}$ relation that we resulted in "bolometric" correlation, we can still clearly see that there is a relation between peak energy and isotropic gamma-ray energy or fluence in "detector band-pass" correlation. Besides peak energy, the integral limits of I depends on the band-pass energy as it is shown in (4.27) and (4.28). Since I is independent of peak energy for the"bolometric" correlation, It can be speculated that the integral for the "detector band-pass" correlation is also independent of peak energy and its deviation from a constant value could be due to the band-pass energy in the integral limit, not peak energy. One source of inacuracy in calculating I comes from the fact that this integral depends on $E_{peak,BB}$ which is equal to DE_{peak}, rather than depending on solely E_{peak}. In our calculations, we consider D to be a constant while it might be different for each GRB. Therefore, a more accurate conclusion can be reached, when D is estimated for each GRB accurately. For now, it can only be deduced that in the "detector band-pass" correlation analysis the $E_{peak}^4 - E_{\gamma,iso}$ relation exists for Swift GRBs with E_{peak} greater than 50 kev and pre-Swift GRBs with E_{peak} greater than 100 kev.

4.4 Conclusion and Future Analysis

Analyzing the thermal component of GRB prompt emission, we have derived two physically motivated correlations for GRB properties. The first one is the correlation between estimated bolometric flux and the calculated thermal flux using the Stephan-Boltzman equation. The next correlation is between estimated

thermal flux in the comoving detector band-pass and the calculated thermal flux in the comoving bandpass by using the Planck function integration. In both relations, Wien's displacement law is applied. The quality of the discussed correlations are comparable with Ghirlanda, E_p-E_γ, relation and provide physical insight to it. These correlations contain three scaling constants. A Monte Carlo test shows that these correlations are independent of the scaling constants.

It is possible to evaluate the three scaling constants. Estimating A, C and D help to examine the discussed correlations more precisely. Based on the Monte Carlo test predication, more acuurate values of the scaling constants should improve the correlations. By determining A, C and D, it is possible to look into the implication of our correlations for Ghrilanda's more closely. The following is how each scaling constant can be approached:

1- D is the ratio of the thermal component peak energy over the prompt emission spectrum peak energy:

$$D = E_{peak,BB}/E_{peak} \tag{4.29}$$

E_{peak} is already known from the Band function fit to the prompt emission spectrum. To find $E_{peak,BB}$, the spectrum first should be fitted to a function with a thermal and a non-thermal component. $E_{peak,BB}$ is the peak energy of thermal component.

2- A is the ratio of the thermal flux over the total flux for a co-moving bandpass:

$$A = F_{BB,[E_1,E_2]}/F_{[E_1,E_2]} \tag{4.30}$$

$F_{BB,[E_1,E_2]}$ can be calculated from integral of the Planck function:

$$F_{BB,[E_1,E_2]} = \pi \int_{E_1}^{E_2} \frac{2E^3/c^2h^3}{exp(chE/kbE_{peak,BB})-1} dE \tag{4.31}$$

where $[E_1, E_2]$ is the co-moving bandpass. This bandpass is $[1, 10^4]$ kev for the "bolometric" relation and $[e_1(1+z), e(1+z)]$ kev for the "detector band-pass" relation. $[e_1, e_2]$ is the detector bandpass. $F_{[E_1,E_2]}$ can be calculated from the integral of the Band function:

$$F_{[E_1,E_2]} = \pi \int_{E_1}^{E_2} \varphi(E)\mathrm{dE} \tag{4.32}$$

$\varphi(E)$ is the Band function. Where

$$\varphi(E) = \begin{cases} \left(\frac{E}{100kev}\right)^{\alpha} exp\left(-\frac{E}{E_0}\right) & (\alpha-\beta)E_0 \geq E \\ \left[\frac{(\alpha-\beta)E_0}{100kev}\right]^{(\alpha-\beta)} exp(\beta-\alpha)\left(\frac{E}{100kev}\right)^{\beta} & (\alpha-\beta)E_0 \leq E \end{cases} \tag{4.33}$$

α is the low energy photon spectral index, β is the high energy photon spectral index and E_0 is the transition energy and equals to $E_{peak}/(2+\alpha)$.

3- C is the scaling constant for photospheric radius estimation.

$$R \cong CR_{\odot} \tag{4.34}$$

where $R_{\odot} = 6.955 \times 10^8 m$. Pe'er et al. (2010b) demonstrate how they use the connection between thermal and non-thermal parts of the spectrum and determine the values of the free model parameters (Lorenz factor, total luminosity of GRB fireball wind and initial radius of GRB, which is defined as the last stable orbit around the central black hole or the sonic radius) and ultimately deduce a Lorentz factor range and photospheric radius. There

are two issues that should be considered if this method is used for photospheric radius estimation. This method results in a range for the radius rather than a constant radius. Also the dependency of the radius on GRB luminosity and its effect in the studied correlations should be examined.

Lastly, here the γ-ray isotropic energy is used in the discussed correlations. Girlanda (2009) shows that using the geometry corrected γ-ray isotropic energy improves the Ghirlanda correlation. Therefore, it is interesting to pursue this study for the geometry corrected isotropic energy and examine the effect of this correction on the discussed correlations.

REFERENCES

Amati, L. et al. 2002, A&A, 390, 81

Band, D. et al. 1993, APJ, 413, 281

Band, D. et al. 1993, APJ, 413, 281

Bloom, J. S. et al. 2001, The Astronomical Journal, 121, 2879

Bloom, J. S.,Frail D. A., & Sari, R. 2003, AJ, 121, 2879

Bloom, J. S.,Frail D. A., & Kulkarni, S. R. 2003, ApJ, 594, 674

Butler, N. R. et al. 2007, ApJ, 671, 656

Carilli, N. Y. et al. 2002, ApJ, 577, 22

Deffayet, C. et al. 2001, Phys. Lett., B502, 199

Deffayet, C. et al. 2002, Phys. Rev., D66, 024019

Dermer, C. D. 1992, Physical Review Letters, 68, 1799

Dvali, G. et al. 2000, Phys. Lett. B485, 208

Frail, D. A. et al. 2001, ApJ, 562, L55

Fishman, G.J., & Meegan, C.A. 1995, ARAA, 33, 415

Fishman, G,. J. 1995, ARA&A, 33,415

Friedman, A. S. et al. 2005, ApJ, 627, 1

Furlanetto S. R. et al. 2002, ApJ, 577,22

Ghirlanda, G., Celotti, A., & Ghisellini, G. 2003, A\&A, 406, 879

Ghirlanda, G. et al. 2004, ApJ, 616, 331

Ghirlanda, G. et al. 2009, preprint (arXiv:0908.1930v1)

Gunn, J. E. et al. 1965, ApJ, 142,1633

Katz, D. et al. 1994, ApJ, 432, L107

Klebesadel, R. et al. 1973, ApJ, 182, L85

Liang, E. et al. 2005, ApJ, 633, 611

Liang, E. et al. 2007, ApJ, 662, 1111

Lithwick, Y. et al. 2001, ApJ, 555, 540

Tavani, M. et al. 1996, ApJ, 466, 768

Mazets, S. V. et al. 1974, JETP Lett., 19, 77

Meegan C. A. et al. 1992, Nature, 355,143

Meszaros P. 1999, !0th October Astrophysics Conference

Meszaros, P., Ramirez-Ruiz, E., Rees, M. J. & Zhang, B. 2002, ApJ, 578, 812

Meszaros, P. et al. 2003, ApJ, 591, L91

Metzger, M. R. et al. 1997, Nature, 387,878

Paciesas, W. S., et al. 1999, APJS, 122, 465

Piran T. 1999, Physics reports, 314, 575

Rhoads, J., E. ApJ, 1997, 487, L1

Pe'er, A. et al. 2010a, ApJ, 614, 827

Pe'er, A. et al. 2010b, preprint (arXiv:1007.2228v1)

Rutledge, R. E. et al. 1995, MNRAS, 276, 753

Ryde, F. et al. 2009, ApJ, 702, 1211

Spergel, D. N. et al. 2007, ApJSS, 170, 377

Stanek, K. Z. et al. 2003, ApJ, 591,L111

Stratta, G. et al. 2009, A&A, 494, L9

Thompson, C. et al. 2007, ApJ, 666, 1012

Zhang, B. et al. 2006, ApJ, 642, 354

Zhang, B. et al. 2007, arXiv:astro-ph/0610177v1